Comput Mech (2011) 48:385–406
DOI 10.1007/s00466-011-0588-3

ORIGINAL PAPER

Exact corotational shell for finite strains and fracture

P. Areias · J. Garção · E. B. Pires · J. Infante Barbosa

Received: 25 August 2010 / Accepted: 9 March 2011 / Published online: 1 April 2011

Abstract The corotational method for frame-invariant elements is generalized to obtain a consistent large-strain shell element incorporating thickness extensibility. The resulting element allows arbitrary in-plane deformations and is distinct from the traditional corotational methods (either quadrature-based or element-based) in the sense that the corotational frame is exact. The polar decomposition operation is performed in two parts, greatly simplifying the linearization calculations. Expressions for the strain-degrees-of-freedom matrices are given for the first time. The symbolic calculations are performed with a well-known algebraic system with a code generation package. Classical linear benchmarks are shown with excellent results. Applications with hyperelasticity and finite strain plasticity are presented, with asymptotically quadratic convergence and very good benchmark results. An example of finite strain plasticity with fracture is solved successfully, showing remarkable robustness without the need of enrichment techniques.

P. Areias (✉) · J. Garção · J. I. Barbosa
Departamento de Física, Colégio Luís António Verney,
Universidade de Évora, Rua Romão Ramalho 59,
7002-554 Évora, Portugal
e-mail: pmaa@uevora.pt; pareias@civil.ist.utl.pt
URL: http://evunix.uevora.pt/~pmaa/

P. Areias · E. B. Pires
ICIST, Lisbon, Portugal

J. Garção · J. I. Barbosa
IDMEC, Lisbon, Portugal

J. Garção
e-mail: jesg@uevora.pt

E. B. Pires
Departamento de Engenharia Civil e Arquitectura, Instituto Superior Técnico, Av. Rovisco Pais, 1049-001 Lisbon, Portugal

Keywords Shells · Finite element · Corotational · Plasticity · Fracture

1 Introduction

Low-order triangular elements are computationally convenient in finite-strain applications since they remain relatively immune to severe mesh distortion;[1] in addition, very efficient algorithms are available to perform remeshing with these elements and the contact detection algorithms are greatly simplified when compared with quadrilaterals. Fracture applications take advantage of the triangular geometry so that robust fracture propagation algorithms are devised [5]. The fracture algorithm is substantially more robust and general than what was long ago performed with intricate extended finite element methods.

High-performance (in the sense of Felippa [20]) small-strain triangles have been devised in the past for both membrane and bending applications [2,10]. Triangle element technology for finite strain elements is comparatively less developed and out-of-plane shell bending applications are also less common. Traditionally, finite-strain triangle elements are created using collapsed four-node elements. In contrast, more disseminated corotational elements are typically applied to problems with large rotations and displacements but small strains. The corotational technique takes advantage of the constant deformation gradient of a membrane triangle to extract the rigid-body displacements from a given element regardless of the underlying element technology. Changes in the element formulation are therefore decoupled from the rigid-body treatment. This favors the encapsula-

[1] Mesh distortion may be caused either by large deformation or by element subdivision in fracture algorithms.

tion of small-strain triangles and the systematic development of high performance procedures without concerns of frame invariance and constitutive modeling with rotations. Furthermore, computational savings are possible without compromise in the applicability in complex problems. Recently, we developed a quadrilateral element with thickness extensibility [7] and attempted to solve finite-strain fracture problems with it.[2] However, it was soon found that algorithm simplicity was greater for triangles, with a moderate accuracy penalty.

Previous limitations of standard corotational techniques are:

- Inadequacy for solving finite strain problems (only finite displacements are allowed).
- Arbitrariness in the choice of the corotational matrix [22].

This work removes these limitations. The paper is organized as follows: we start by deriving the exact corotational kinematics for a 3 node triangle in Sect. 2; then the bending and membrane formulations of the core element are derived in Sect. 3. A simplified version of our recent work [7] for thickness variation is presented in Sect. 4. Finally, we present two verification tests showing the exactness of the proposed corotational frame and a number of benchmark tests, including one involving multiple fracture of a simply-supported square plate with finite strain plasticity. Conclusions are drawn in Sect. 6.

2 Governing equations and exact corotational kinematics for a 3 node triangle

The problem under study is the equilibrium problem of a continuous medium (see, e.g. [3]). The specific shell kinematics (see for example [7,13]) do not impose distinction with the continuum. In the present context, director constraints are satisfied at the discrete level. The equations in weak form are given by [25]:

Given $b : \Omega \to \mathbb{R}^3$, $\boldsymbol{t} : \Gamma_{\overline{t}} \to \mathbb{R}^3$ and $\overline{\boldsymbol{u}} : \Gamma_{\overline{u}} \to \mathbb{R}^3$, find $\boldsymbol{u} \in \mathscr{D} | \forall \delta \boldsymbol{u} \in \mathscr{V}$ solving:

$$\int_\Omega \boldsymbol{\sigma} : \nabla \delta \boldsymbol{u} \mathrm{d}\Omega = \int_\Omega \boldsymbol{b} \cdot \delta \boldsymbol{u} \mathrm{d}\Omega + \int_{\Gamma_{\overline{t}}} \boldsymbol{t} \cdot \delta \boldsymbol{u} \mathrm{d}\Gamma \tag{1}$$

$$\boldsymbol{u} = \overline{\boldsymbol{u}} \quad \text{on} \quad \Gamma_{\overline{u}} \tag{2}$$

$$\delta \boldsymbol{u} = \boldsymbol{0} \quad \text{on} \quad \Gamma_{\overline{u}} \tag{3}$$

where $\boldsymbol{u}$ is the unknown displacement vector field, $\delta \boldsymbol{u}$ is the test field and $\boldsymbol{\sigma}$ is the Cauchy stress tensor. Ω (the body) is a open set where $\boldsymbol{b}$ (the body forces) and $\boldsymbol{\sigma}$ (the Cauchy stress) are defined. The gradient operator ∇ is taken with respect to deformed coordinates.

The boundary of Ω is the union of $\Gamma_{\overline{t}}$ (the natural boundary, with $\boldsymbol{t}$ known) and $\Gamma_{\overline{u}}$ (the essential boundary with $\overline{\boldsymbol{u}}$ known). The set $\mathscr{D}$ of the trial functions is defined as: $\mathscr{D} = \{\boldsymbol{u} | \boldsymbol{u} \in [\mathscr{H}^1(\Omega)]^3, \boldsymbol{u} = \overline{\boldsymbol{u}} \text{ on } \Gamma_{\overline{u}}\}$. The set of the test functions is defined as $\mathscr{V} = \{\delta \boldsymbol{u} | \delta \boldsymbol{u} \in [\mathscr{H}^1(\Omega)]^3, \delta \boldsymbol{u} = \boldsymbol{0} \text{ on } \Gamma_{\overline{u}}\}$. $[\mathscr{H}^1(\Omega)]^3$ is the product of Sobolev spaces of order 1.

The weak form of equilibrium (1) is approximately satisfied by discretization with triangular shell elements. The director constraints and the discrete form of equilibrium are formulated in a corotational frame, in the sense of Felippa and Haugen [22].

For a three-node triangle embedded in $\mathbb{R}^3$ it is possible to calculate the unique rotation matrix from the polar decomposition, avoiding ad-hoc corotational frames. This fact is well known by the element technology community, but for a 3×3 deformation gradient it becomes too costly, particularly if second derivatives (with respect to $\boldsymbol{u}$) are required for application with Newton's method of solution. Since a simple closed-form solution exists for 2×2 matrices, a less costly (but producing the exact result) derivation is presented here. It is discontinuity free and well-posed. It consists of a geometrical construction which in the end allows a bidimensional polar decomposition. This geometrical construction is *exact* and greatly reduces the effort required to perform a full $3D$ polar decomposition. It is worth realizing that it is common to estimate the rotation matrix by empirical methods. During the last three decades there have been several proposals, some of which can lead to spurious loss of symmetry, fictitious rotations and energy dissipation in closed cycle. The latest corotational frames, widely used in more recent papers and commercial codes, are the ones obtained by either:

- Minimizing the average distance between rigidly rotated and deformed nodes. It can be shown that it is exact for rigid body motions, it is independent of node numbering and retains isotropy. However it produces fictitious rotations, as we shall see (also demonstrated in [11]).
- Making use of the null drilling part of the local spin as a replacement of the exact polar decomposition [17].

both are *unsatisfactory*. Often they appear to work flawlessly in one or two-element tests since for certain nodal arrangements the defects will not surface. In Sect. 5.1 we show a specific nodal arrangement exposing the deficiencies of these two corotational frames. Our alternative approach to corotational kinematics has the goal of solving finite strain problems with triangular shells. Exact derivatives are used (separately calculated with Mathematica [32] and the

[2] Note that director kinematics is, in general, dependent on the constitutive law, as shown in that work.

AceGen add-on [29]) and therefore quadratic convergence is obtained.

Let us consider the pseudo-time $t \in \mathbb{R}_0^+$ as a scale to register motion events. Given a triangle (for practical purposes identified as $\mathscr{T}$) subject to a homogeneous deformation, let us consider a given point $X \in \mathscr{T}$ and the associated deformed $\boldsymbol{x}_X$ and undeformed $\boldsymbol{X}_X$ positions. The undeformed position is a specialization of the deformed one, since $\boldsymbol{X}_X = \boldsymbol{x}_X|_{t=0}$. The difference between these positions is the displacement vector, $\boldsymbol{u}_X$ which can be decomposed into deformation (d) and rigid (r) terms. The deformation displacement $\boldsymbol{u}_X^d$ is given by the difference between the total displacement $\boldsymbol{u}_X$ and the rigid body displacement $\boldsymbol{u}_X^r$:

$$\boldsymbol{u}_X^d = \boldsymbol{u}_X - \boldsymbol{u}_X^r \tag{4}$$

Since the deformation gradient is unaltered by a rigid body translation, we can arbitrarily select a point as a frame origin. We use the triangle centroid in a given configuration as the frame origin. The centroid has deformed coordinates $\boldsymbol{x}_C$ and undeformed coordinates $\boldsymbol{X}_C = \boldsymbol{x}_C|_{t=0}$; the difference is the centroid's displacement vector $\boldsymbol{u}_C = \boldsymbol{x}_C - \boldsymbol{X}_C$. Therefore, we establish, for a given point X, the *shifted* undeformed coordinates and deformed coordinates as:

$$\boldsymbol{X}_{sX} = \boldsymbol{X}_X - \boldsymbol{X}_C \tag{5}$$

$$\boldsymbol{x}_{sX} = \boldsymbol{x}_X - \boldsymbol{x}_C \tag{6}$$

The corresponding shifted displacement, $\boldsymbol{u}_{sX}$ is therefore determined by their difference:

$$\boldsymbol{u}_{sX} = \boldsymbol{x}_{sX} - \boldsymbol{X}_{sX} = \boldsymbol{u}_X - \boldsymbol{u}_C \tag{7}$$

According to its definition, the deformation gradient is the derivative of $\boldsymbol{x}_{sX}$ with respect to $\boldsymbol{X}_{sX}$:

$$\boldsymbol{F} = \frac{\partial \boldsymbol{x}_{sX}}{\partial \boldsymbol{X}_{sX}} \tag{8}$$

The deformed position $\boldsymbol{x}_X$ (and similarly the total displacement $\boldsymbol{u}_X$) of any point $X \in \mathscr{T}$ can be obtained by a linear combination of the triangle corner positions $\boldsymbol{x}_i$ or displacements $\boldsymbol{u}_i, i = 1, 2, 3$. Consequently the deformation gradient $\boldsymbol{F}$ is constant and can be written solely in terms of the triangle corner positions $\boldsymbol{x}_i, \boldsymbol{X}_i$ (or displacements $\boldsymbol{u}_i$). Introducing the rotation matrix, $\boldsymbol{R} = \boldsymbol{F}\left(\boldsymbol{F}^T\boldsymbol{F}\right)^{-1/2}$ resulting from the polar decomposition, and using Chasles corollary (cf. [24]), the rigid body displacement is obtained by the rotation of $\boldsymbol{X}_{sX}$[3]:

$$\boldsymbol{u}_{sX}^r = (\boldsymbol{R} - \boldsymbol{I})\,\boldsymbol{X}_{sX} \tag{9}$$

The validity of equation (9) stems from $\boldsymbol{F}$ and therefore $\boldsymbol{R}$ being uniform in each element. With this conclusion, we calculate the deformation displacement as a difference:

$$\boldsymbol{u}_{sX}^d = \boldsymbol{u}_{sX} - (\boldsymbol{R} - \boldsymbol{I})\boldsymbol{X}_{sX} \tag{10}$$

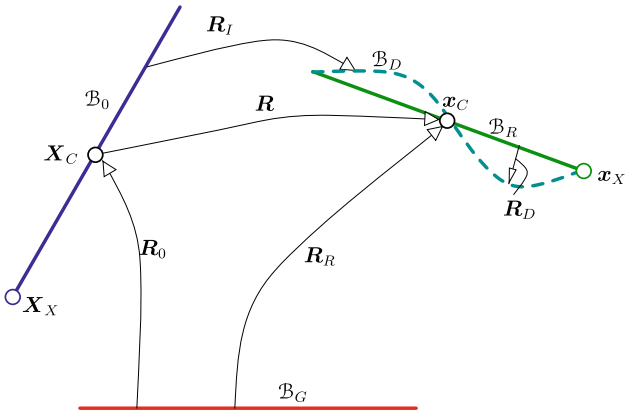

Fig. 1 General notation for the corotational decomposition, using a beam to facilitate the interpretation

The rotation matrix, $\boldsymbol{R}$, which is uniform for the given triangle, is the non-deformation part of the total rotation. In beams and shells, mid-surface and drilling rotation are strain-producing and will also be accounted for. In particular, for an element with nodal rotation degrees of freedom, the corresponding deformation from the reference configuration can be expressed using a total rotation tensor $\boldsymbol{R}_I$. The rotation-induced deformation that an element actually *experiences* is here designated by $\boldsymbol{R}_D$ which also depends in general of the point considered. Using the notation shown in Fig. 1 we obtain the rigid body rotation by extracting the deformation rotation ($\boldsymbol{R}_D$) from the total rotation $\boldsymbol{R}_I$:

$$\boldsymbol{R} = \boldsymbol{R}_D^T\boldsymbol{R}_I \tag{11}$$

This establishes the rigid body rotation $\boldsymbol{R}$, which is uniform,[4] as a product of two non-uniform matrices. To the rotated frame we associate the rotation matrix $\boldsymbol{R}_R = \boldsymbol{R}\boldsymbol{R}_0$ which is also uniform. Using the transpose of this matrix as a transformation along with decomposition (11) we can write the uniform membrane deformation displacement in the frame $\mathscr{B}_R$ by pre-multiplying $\boldsymbol{u}_X^d$ by $\boldsymbol{R}_R^T$:

$$\overline{\boldsymbol{u}}_{sX}^d = \boldsymbol{R}_R^T\boldsymbol{x}_{sX} - \boldsymbol{R}_0^T\boldsymbol{X}_{sX} \tag{12}$$

where use was made of the *alibi-alias* duality and matrix orthogonality. Corresponding to this deformational displacement we have the undeformed and deformed coordinates in the same frame $\mathscr{B}_R$:

$$\overline{\boldsymbol{X}}_{sX} = \boldsymbol{R}_0^T\boldsymbol{X}_{sX} \tag{13}$$

$$\overline{\boldsymbol{x}}_{sX} = \boldsymbol{R}_R^T\boldsymbol{x}_{sX} \tag{14}$$

[3] Note that the displacement of the centroid is included in $\boldsymbol{u}_{sX}$ and $\boldsymbol{u}_{sX}^r = \boldsymbol{u}_X^r - \boldsymbol{u}_C$.

[4] In the sense that their components do not vary in each triangle.

This *differs* from the classical approach for deriving corotational elements since the nodal positions allow the use of large strain formulations based on a rotation-free deformation gradient. It is only possible to perform that operation if $\boldsymbol{R}_R$ is exactly calculated. To the Authors' knowledge, this calculation is performed here for the first time. The deformational rotation matrix ($\boldsymbol{R}_D$ in Fig. 1) can also be given by $\boldsymbol{R}_D = \boldsymbol{R}_I \boldsymbol{R}_0 \boldsymbol{R}_R^T$ or in the frame $\mathscr{B}_R$, as the back-rotated $\boldsymbol{R}_D$:

$$\overline{\boldsymbol{R}}_D = \boldsymbol{R}_R^T \boldsymbol{R}_I \boldsymbol{R}_0 \tag{15}$$

The quantities $\overline{\boldsymbol{u}}_{sX}^d$ and $\overline{\boldsymbol{R}}_D$ are used by the encapsulated (linear) element as measures of deformational displacement and rotation, respectively. Thus the corotational derivation is defined in terms of:

1. The total rotation matrix for frame $\mathscr{B}_R$, $\boldsymbol{R}_R$ and the specialization for frame $\mathscr{B}_0$, $\boldsymbol{R}_0$.
2. The nodal rotation matrix $\boldsymbol{R}_I$.

Since other relevant quantities lie solely on these two rotation matrices, it becomes clear the importance given to the topic in the literature (see, e.g. [17]).

2.1 Calculation of $\boldsymbol{R}_R$

Matrix $\boldsymbol{R}_R$ defines $\mathscr{B}_R$, which is often identified as the "local element frame" in the literature. The calculation of $\boldsymbol{R}_R$ involves a number of steps which we now show in detail. Matrix $\boldsymbol{R}_0$ can be obtained by a frame attached to $\mathscr{B}_0$ and does not affect the results, since the reference configuration is arbitrary. For simplicity, one of the frame's axis is orthogonal to the triangle (Fig. 2). Given $\boldsymbol{R}_0$, the total rotation matrix $\boldsymbol{R}_R$ can be obtained as:

$$\boldsymbol{R}_R = \boldsymbol{R}\boldsymbol{R}_0 \tag{16}$$

with $\boldsymbol{R}$ being generally provided in other works [11,17] by an *approximation* to the polar decomposition of $\boldsymbol{F}$. The rotation matrix $\boldsymbol{R}_R$ can also be given by the following relation:

$$\boldsymbol{R}_R = \boldsymbol{R}_E \boldsymbol{R}_F \tag{17}$$

where $\boldsymbol{R}_E$ is a rotation matrix derived from the deformed corner nodal positions $\boldsymbol{x}_i$ and $\boldsymbol{R}_F$ is a rotation matrix obtained by polar decomposition of a local $\mathscr{B}_R$ two-dimensional deformation gradient $\boldsymbol{F}^\star$. The columns of the rotation matrix $\boldsymbol{R}_E$ are the basis vectors of frame $\mathscr{B}_E$ (see Fig. 2):

$$\boldsymbol{R}_E = \left[\boldsymbol{e}_1' | \boldsymbol{e}_2' | \boldsymbol{e}_3'\right] \tag{18}$$

so that $\boldsymbol{x}_{sX}' = \boldsymbol{R}_E^T \boldsymbol{x}_{sX}$. The basis vectors $\boldsymbol{e}_i'$, $i = 1, 2, 3$ are obtained by the following relations (analogous relations are used in the determination of $\boldsymbol{R}_0$ but using the undeformed corner nodal positions $\boldsymbol{X}_i$):

$$\boldsymbol{e}_1' = (\boldsymbol{x}_2 - \boldsymbol{x}_1) / \|\boldsymbol{x}_2 - \boldsymbol{x}_1\| \tag{19}$$

$$\boldsymbol{e}_2' = \boldsymbol{e}_3' \times \boldsymbol{e}_1' \tag{20}$$

$$\boldsymbol{e}_3' = (\boldsymbol{x}_2 - \boldsymbol{x}_1) \times (\boldsymbol{x}_3 - \boldsymbol{x}_1) / \|(\boldsymbol{x}_2 - \boldsymbol{x}_1) \times (\boldsymbol{x}_3 - \boldsymbol{x}_1)\| \tag{21}$$

Since the choice of $\boldsymbol{e}_i'$ (and therefore $\boldsymbol{R}_E$) is arbitrary and the calculation of $\boldsymbol{R}_R$ is not, $\boldsymbol{R}_F$ will depend on this choice. If three configurations are drawn with coincident frames (see Fig. 2) we obtain the rotation matrix $\boldsymbol{R}_F$ as an extension of a 2×2 rotation matrix obtained by polar decomposition of the local deformation gradient:

$$\boldsymbol{R}_F = \begin{bmatrix} \boldsymbol{R}^\star & 0 \\ 0 & 1 \end{bmatrix} \tag{22}$$

$$\boldsymbol{R}^\star = \boldsymbol{F}^\star \left(\boldsymbol{F}^{\star T} \boldsymbol{F}^\star\right)^{-\frac{1}{2}} \tag{23}$$

With the notation depicted in Fig. 2 we calculate the undeformed $\boldsymbol{J}_0$ and deformed $\boldsymbol{J}$ Jacobians, using a three node linear parametrization (2×2 matrices whose columns are corner nodes relative position vectors aligned to the element edges). For the in-plane motion, the 2×2 matrices $\boldsymbol{J}_0$ and $\boldsymbol{J}$ are given by:

$$\boldsymbol{J}_0 = \left[\overline{\boldsymbol{X}}_{s1} - \overline{\boldsymbol{X}}_{s3} | \overline{\boldsymbol{X}}_{s2} - \overline{\boldsymbol{X}}_{s3}\right] \tag{24}$$

$$\boldsymbol{J} = \left[\boldsymbol{x}_{s1}' - \boldsymbol{x}_{s3}' | \boldsymbol{x}_{s2}' - \boldsymbol{x}_{s3}'\right] \tag{25}$$

The local 2×2 deformation gradient $\boldsymbol{F}^\star$ is calculated using the definition and the chain rule of derivation:

$$\boldsymbol{F}^\star = \boldsymbol{J}\boldsymbol{J}_0^{-1} \tag{26}$$

Given the bidimensional part of the deformation gradient $\boldsymbol{F}^\star$, $\det \boldsymbol{F}^\star > 0$ we perform a polar decomposition which reads:

$$\boldsymbol{F}^\star = \boldsymbol{R}^\star \boldsymbol{U}^\star \tag{27}$$

where $\boldsymbol{R}^\star$ is a proper orthogonal matrix and $\boldsymbol{U}^\star$ is a symmetric positive-definite matrix. Standard arithmetic provides the rotation angle as[5]:

$$\gamma = \arctan\left(\frac{F_{21}^\star - F_{12}^\star}{F_{11}^\star + F_{22}^\star}\right) \tag{28}$$

with

$$\boldsymbol{R}^\star = \begin{bmatrix} \cos\gamma & -\sin\gamma \\ \sin\gamma & \cos\gamma \end{bmatrix} \tag{29}$$

Therefore, the polar decomposition is performed in two parts:

1. Mapping to a frame where 2×2 matrices suffice (after (16) and (17)).

[5] The two-argument arctan function is used.

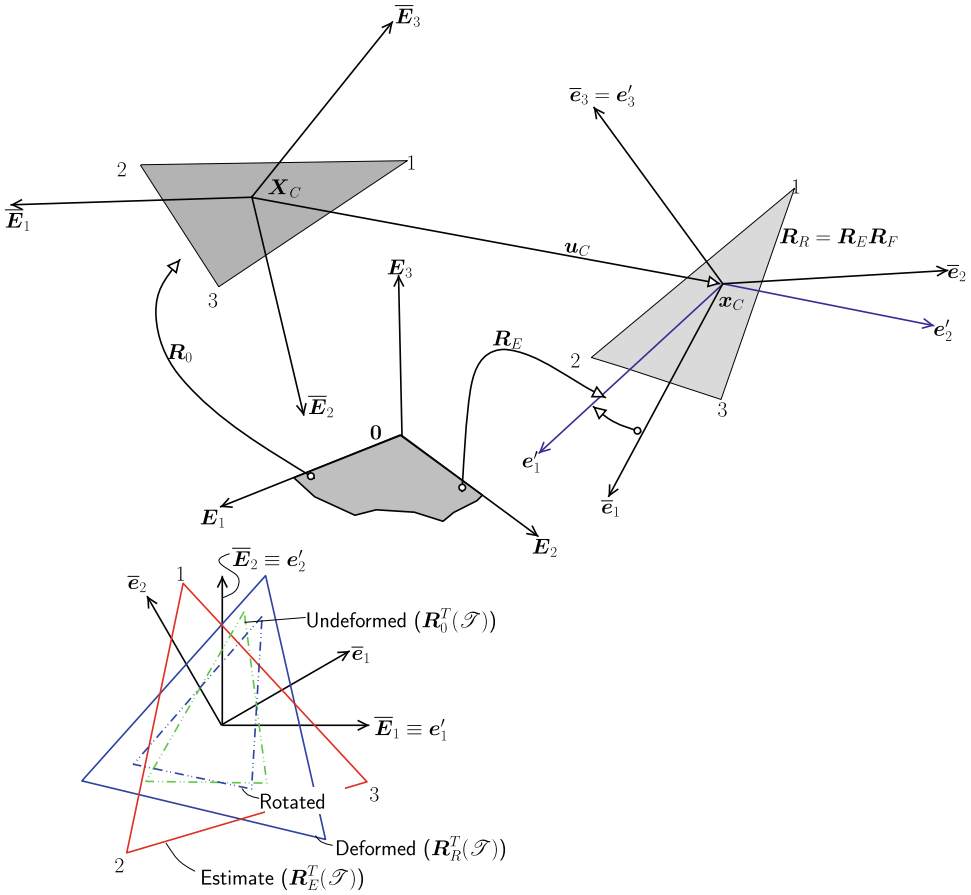

Fig. 2 Corotational notation for a triangle. Note that the frames are provided by the orthogonal matrices $\boldsymbol{R}_E = [\boldsymbol{e}'_1|\boldsymbol{e}'_2|\boldsymbol{e}'_3]$, $\boldsymbol{R}_0 = [\overline{\boldsymbol{E}}_1|\overline{\boldsymbol{E}}_2|\overline{\boldsymbol{E}}_3]$ and $\boldsymbol{R}_R = [\overline{\boldsymbol{e}}_1|\overline{\boldsymbol{e}}_2|\overline{\boldsymbol{e}}_3]$. In the *lower part* of the Figure, we overlap the configurations by imposing $\overline{\boldsymbol{E}}_i \equiv \boldsymbol{e}'_i$ so that relative stretches and rotations can be observed

2. Calculation of a single angle in 2D, which is sufficient to determine the rotation matrix in that frame (equations (27), (28) and (29)). These quantities are then used to obtain $\boldsymbol{R}$.

To prove the exactness of equation (17) we start by making use of two auxiliary vectors, say $\boldsymbol{w}_0$ and $\boldsymbol{w}_n$ where $\boldsymbol{w}_n = \boldsymbol{R}\boldsymbol{w}_0$, i.e. $\boldsymbol{w}_n$ is the image of $\boldsymbol{w}_0$ under a rotation (the alibi). Performing the change of frame of representation (alias) we obtain:

$$\overline{\boldsymbol{w}}_0 = \boldsymbol{R}_0^T \boldsymbol{w}_0 \tag{30}$$
$$\boldsymbol{w}'_n = \boldsymbol{R}_E^T \boldsymbol{w}_n \tag{31}$$

Rotating $\boldsymbol{w}'_n$ by $\boldsymbol{R}_F$ and transposing we isolate $\boldsymbol{w}_n$ in the left-hand-side:

$$\boldsymbol{w}_n = \boldsymbol{R}_E \boldsymbol{R}_F \boldsymbol{R}_0^T \boldsymbol{w}_0 \tag{32}$$

Using definition (16) we write (32) as:

$$\boldsymbol{w}_n = \boldsymbol{R}\boldsymbol{w}_0 \tag{33}$$

which implies that $\boldsymbol{R}_R = \boldsymbol{R}_E \boldsymbol{R}_F$. This equation is exact and therefore $\boldsymbol{R}_R$ is also the *exact* rotation. Our first example further verifies this statement. The first and second variations of $\boldsymbol{R}_R$ are given by:

$$\delta \boldsymbol{R}_R = \delta \boldsymbol{R}_E \boldsymbol{R}_F + \boldsymbol{R}_E \delta \boldsymbol{R}_F \tag{34}$$
$$\mathrm{d}\delta \boldsymbol{R}_R = \mathrm{d}\delta \boldsymbol{R}_E \boldsymbol{R}_F + \delta \boldsymbol{R}_E \mathrm{d}\boldsymbol{R}_F \tag{35}$$
$$+ \boldsymbol{R}_E \mathrm{d}\delta \boldsymbol{R}_F + \mathrm{d}\boldsymbol{R}_E \delta \boldsymbol{R}_F \tag{36}$$

these are exactly calculated using Mathematica [32] with the Acegen add-on [29].

2.2 Membrane stretch

The polar decomposition of the membrane deformation gradient is written as $\boldsymbol{F} = \boldsymbol{R}\boldsymbol{U}$ with $\boldsymbol{U}$ being the right stretch tensor. Writing $\boldsymbol{F}$ in terms of the local $\mathscr{B}_0$ and $\mathscr{B}_R$ frames provides:

$$\overline{\boldsymbol{F}} = \boldsymbol{R}_R^T \boldsymbol{F} \boldsymbol{R}_0 = \boldsymbol{R}_0^T \boldsymbol{U} \boldsymbol{R}_0$$
$$\Leftrightarrow \overline{\boldsymbol{F}} = \overline{\boldsymbol{U}} \tag{37}$$

therefore the deformation gradient in frame $\mathscr{B}_0$ is rotation-free and equals the stretch. Analogous arguments lead to $\overline{\boldsymbol{F}} = \boldsymbol{R}_R^T \boldsymbol{V} \boldsymbol{R}_R = \overline{\boldsymbol{V}}$, so that:

$$\boldsymbol{F} = \begin{cases} \overline{\boldsymbol{U}} & \text{in } \mathscr{B}_0 \\ \overline{\boldsymbol{V}} & \text{in } \mathscr{B}_R \end{cases} \tag{38}$$

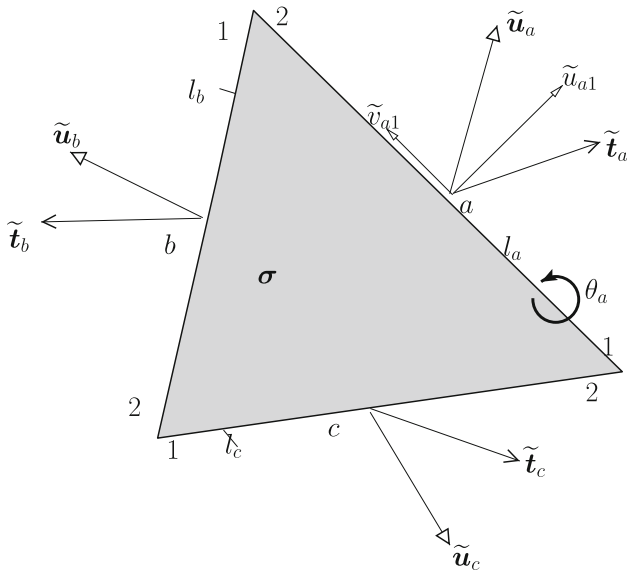

Fig. 3 Notation for the edge interpolation of the membrane part. Edge a is detailed

Consequently, for the element embedded in the corotated frame, just the membrane stretch is visible. The long standing restriction to small strains is definitely removed.

Remark 1 Given a triangle $\mathscr{T}$ embedded in $\mathbb{R}^3$ with two configurations $\mathscr{B}_0$ and $\mathscr{B}_D$, whose deformation deformation gradient is $\boldsymbol{F}$ in the frame $\mathscr{B}_G$, then there are two frames, $\mathscr{B}_0$ and $\mathscr{B}_R$ in which $\boldsymbol{F}$ is reduced to a right and left stretch, respectively: $\overline{\boldsymbol{U}} = \boldsymbol{R}_0 \overline{\boldsymbol{F}} \boldsymbol{R}_0^T$, $\overline{\boldsymbol{V}} = \boldsymbol{R}_R \overline{\boldsymbol{F}} \boldsymbol{R}_R^T$.

2.3 Displacement calculation

If the undeformed triangle coordinates (in $\mathscr{B}_G$) are organized as lines of matrices (here $\boldsymbol{T}_x$ and $\boldsymbol{T}_X$) then we will obtain the transformed coordinates (in $\mathscr{B}_R$) by matrix multiplication. Let us introduce the two matrices in $\mathscr{B}_G$:

$$\boldsymbol{T}_x = \begin{bmatrix} \boldsymbol{x}_1 \\ \boldsymbol{x}_2 \\ \boldsymbol{x}_3 \end{bmatrix} \tag{39}$$

$$\boldsymbol{T}_X = \begin{bmatrix} \boldsymbol{X}_1 \\ \boldsymbol{X}_2 \\ \boldsymbol{X}_3 \end{bmatrix} \tag{40}$$

then the shifted (s) coordinate coordinate matrices for $\mathscr{B}_R$ are simply given by:

$$\boldsymbol{T}_{s\overline{x}} = \begin{bmatrix} \overline{\boldsymbol{x}}_{s1} \\ \overline{\boldsymbol{x}}_{s2} \\ \overline{\boldsymbol{x}}_{s3} \end{bmatrix} = \boldsymbol{T}_x \boldsymbol{P} \boldsymbol{R}_R \tag{41}$$

$$\boldsymbol{T}_{s\overline{X}} = \begin{bmatrix} \overline{\boldsymbol{X}}_{s1} \\ \overline{\boldsymbol{X}}_{s2} \\ \overline{\boldsymbol{X}}_{s3} \end{bmatrix} = \boldsymbol{T}_X \boldsymbol{P} \boldsymbol{R}_0 \tag{42}$$

with the projection linear transformation:

$$\boldsymbol{P} = \frac{1}{3} \begin{bmatrix} 2 & -1 & -1 \\ -1 & 2 & -1 \\ -1 & -1 & 2 \end{bmatrix} \tag{43}$$

providing the element centroid coordinates.[6] Making use of $\boldsymbol{T}_{s\overline{u}} = \boldsymbol{T}_{s\overline{x}} - \boldsymbol{T}_{s\overline{X}}$, the nodal deformation displacements are calculated by linear algebra in the local corotated frame. The first and second variation of $\boldsymbol{T}_{sx}$, required for the Newton's method of solution, are consequences of these results:

$$\delta \boldsymbol{T}_{s\overline{x}} = \delta \boldsymbol{T}_x \boldsymbol{P} \boldsymbol{R}_R + \boldsymbol{T}_x \boldsymbol{P} \delta \boldsymbol{R}_R \tag{44}$$

$$\mathrm{d}\delta \boldsymbol{T}_{s\overline{x}} = \mathrm{d}\delta \boldsymbol{T}_x \boldsymbol{P} \boldsymbol{R}_R + \delta \boldsymbol{T}_x \boldsymbol{P} \mathrm{d}\boldsymbol{R}_R \tag{45}$$

$$+ \mathrm{d}\boldsymbol{T}_x \boldsymbol{P} \delta \boldsymbol{R}_R + \boldsymbol{T}_x \boldsymbol{P} \mathrm{d}\delta \boldsymbol{R}_R \tag{46}$$

2.4 Calculation of $\boldsymbol{R}_I$

The non-uniform part of $\overline{\boldsymbol{R}}_D$, which we denote $\boldsymbol{R}_I$, is obtained at each node K from four nodal Euler parameters $\boldsymbol{q}_K = \{q_{K0}, q_{K1}, q_{K2}, q_{K3}\}^T$; $\boldsymbol{R}_I(\boldsymbol{q}_K)$ is the following function:

$$\boldsymbol{R}_I(\boldsymbol{q}_K) = \begin{bmatrix} 1-2\left(q_{K2}^2+q_{K3}^2\right) & 2(q_{K1}q_{K2}-q_{K0}q_{K3}) & 2(q_{K0}q_{K2}+q_{K1}q_{K3}) \\ 2(q_{K1}q_{K2}+q_{K0}q_{K3}) & 1-2(q_{K1}^2+q_{K3}^2) & 2(q_{K2}q_{K3}-q_{K0}q_{K1}) \\ 2(q_{K1}q_{K3}-q_{K0}q_{K2}) & 2(q_{K0}q_{K1}+q_{K2}q_{K3}) & 1-2(q_{K1}^2+q_{K2}^2) \end{bmatrix} \tag{47}$$

with $q_{K0}^2+q_{K1}^2+q_{K2}^2+q_{K3}^2 = 1$ being the Euler parameters' constraint. From the alternative rotation parametrizations, this has several known advantages, discussed at length in various papers (see, e.g. [16]). First and second derivatives of $\boldsymbol{R}_I$ with respect to $\boldsymbol{q}_K$ are straightforward and were performed by Mathematica [32] with the Acegen add-on [29]. The matrices $\boldsymbol{R}_I(\boldsymbol{q}_K)$, $K = 1, 2, 3$ and $\boldsymbol{R}_D(\boldsymbol{q}_K)$, $K = 1, 2, 3$ are calculated from (47) and (15) after the calculation of $\boldsymbol{R}_R$ in (17). We calculate the local nodal deformational displacement $\overline{\boldsymbol{u}}_K^d$ and deformational rotation $\overline{\boldsymbol{\theta}}_K^d$ in the frame $\mathscr{B}_R$. From the deformational rotation matrix we extract the rotation vector by well-known eigenvalue analysis (cf. [24]):

$$2\cos(\overline{\theta}_K^d) + 1 = \mathrm{tr}(\overline{\boldsymbol{R}}_D) \tag{48}$$

$$\overline{\boldsymbol{\theta}}_K^d = \frac{\overline{\theta}_K^d}{2\sin\overline{\theta}_K^d} \begin{Bmatrix} \overline{R}_{D32}(\boldsymbol{q}_K) - \overline{R}_{D23}(\boldsymbol{q}_K) \\ \overline{R}_{D13}(\boldsymbol{q}_K) - \overline{R}_{D31}(\boldsymbol{q}_K) \\ \overline{R}_{D21}(\boldsymbol{q}_K) - \overline{R}_{D12}(\boldsymbol{q}_K) \end{Bmatrix} \tag{49}$$

[6] This linear transformation is analogous to the deviatoric projection in small strain elasticity.

The first and second variation of $\overline{\boldsymbol{\theta}}^d_K$ are given by the application of the chain rule (now omitting the nodal unknowns):

$$\delta\overline{\boldsymbol{\theta}}^d_K = \overline{\boldsymbol{\theta}}^{d'}_K : \left[\delta \boldsymbol{R}^T_R \boldsymbol{R}_I \boldsymbol{R}_0 + \boldsymbol{R}^T_R \delta \boldsymbol{R}_I \boldsymbol{R}_0\right] \tag{50}$$

$$\begin{aligned}\mathrm{d}\delta\overline{\boldsymbol{\theta}}^d_K = \overline{\boldsymbol{\theta}}^{d'}_K : \Big[&\mathrm{d}\delta \boldsymbol{R}^T_R \boldsymbol{R}_I \boldsymbol{R}_0 + \boldsymbol{R}^T_R \mathrm{d}\delta \boldsymbol{R}_I \boldsymbol{R}_0 \\ &+\delta \boldsymbol{R}^T_R \mathrm{d}\boldsymbol{R}_I \boldsymbol{R}_0 + \mathrm{d}\boldsymbol{R}^T_R \delta \boldsymbol{R}_I \boldsymbol{R}_0\Big] \\ &+\Big[\delta \boldsymbol{R}^T_R \boldsymbol{R}_I \boldsymbol{R}_0 + \boldsymbol{R}^T_R \delta \boldsymbol{R}_I \boldsymbol{R}_0\Big] : \overline{\boldsymbol{\theta}}^{d''}_K : \Big[\mathrm{d}\boldsymbol{R}^T_R \boldsymbol{R}_I \boldsymbol{R}_0 \\ &+\boldsymbol{R}^T_R \mathrm{d}\boldsymbol{R}_I \boldsymbol{R}_0\Big]\end{aligned} \tag{51}$$

In addition, we also adopt the exact incremental procedure proposed by Brank and Ibrahimbegovic [16] to avoid the undefined sign for large values of the Euler parameters. This requires storage of previous rotation matrices.

2.5 Complete transformation map and consistent linearization

Each node is associated with three displacement degrees of freedom and three rotation parameters in the frame $\mathscr{B}_G$. We group these as

$$\boldsymbol{v}_K = \{u_{K1}, u_{K2}, u_{K3}, q_{K1}, q_{K2}, q_{K3}\}^T, \quad K = 1, 2, 3 \tag{52}$$

Juxtaposing each nodal set of degrees of freedom we obtain:

$$\boldsymbol{v} = \{\boldsymbol{v}_1, \boldsymbol{v}_2, \boldsymbol{v}_3\}^T \tag{53}$$

In the frame $\mathscr{B}_R$ we can write:

$$\overline{\boldsymbol{v}}_K = \{\overline{u}_{dK1}, \overline{u}_{dK2}, \overline{u}_{dK3}, \overline{q}_{K1}, \overline{q}_{K2}, \overline{q}_{K3}\}^T \tag{54}$$

and

$$\overline{\boldsymbol{v}} = \{\overline{\boldsymbol{v}}_1, \overline{\boldsymbol{v}}_2, \overline{\boldsymbol{v}}_3\}^T \tag{55}$$

Using the mapping $\mathbb{R}^{16} \ni \boldsymbol{v} \to \boldsymbol{\varphi}(\boldsymbol{v}) = \overline{\boldsymbol{v}} \in \mathbb{R}^{16}$ we can write:

$$\overline{\boldsymbol{v}} = \boldsymbol{\varphi}(\boldsymbol{v}) \tag{56}$$

Given the force in frame $\mathscr{B}_R$, $\overline{\boldsymbol{f}}$, we can use energy conjugacy to obtain the force in frame $\mathscr{B}_0$, denoted as $\boldsymbol{f}$:

$$\boldsymbol{f} = \left(\frac{\mathrm{d}\boldsymbol{\varphi}(\boldsymbol{v})}{\mathrm{d}\boldsymbol{v}}\right)^T \overline{\boldsymbol{f}} \tag{57}$$

or, in index notation,

$$f_j = \frac{\mathrm{d}\varphi_i}{\mathrm{d}v_j}\overline{f}_i \tag{58}$$

and the stiffness in frame $\mathscr{B}_0$ is given, in index notation, by:

$$K_{ik} = \frac{\mathrm{d}\varphi_j(\boldsymbol{v})}{\mathrm{d}v_i}\frac{\mathrm{d}\varphi_l(\boldsymbol{v})}{\mathrm{d}v_k}\overline{K}_{jl} + \overline{f}_j\frac{\mathrm{d}^2\varphi_j(\boldsymbol{v})}{\mathrm{d}v_i\mathrm{d}v_k} \tag{59}$$

where $\overline{K}_{jl}$ is the local stiffness matrix. Optimized expressions for the first and second derivatives of $\varphi(\boldsymbol{v})$ were calculated using Mathematica with the AceGen add-on. We omit these here for conciseness, but the generated code can be obtained from the first Author. Part of the the calculations correspond to equations (34) and (44). The Cauchy stress in frame $\mathscr{B}_0$ is determined by the corotational transformation of the rotated stress $\overline{\boldsymbol{\sigma}}$[7]:

$$\boldsymbol{\sigma} = \boldsymbol{R}_0 \overline{\boldsymbol{\sigma}} \boldsymbol{R}^T_0 \tag{60}$$

3 Core element matrices

Here we adopted a flat 3 node shell triangle constructed by assembling a modified membrane element (OPT) with drilling degrees of freedom, with a re-derived plate element (DKT). These are generalized for arbitrarily large strains and can cope with hyperelastic and hyperelastic/plastic materials. Besides the in-plane bending mode, the drilling degrees-of-freedom allow the treatment of general shell intersections and also connections to beam elements, making the element adequate to model an extended range of structures. Since the rotation tensor $\boldsymbol{R}$ was removed by the use of frame $\mathscr{B}_R$, the right stretch can be written in the frame $\mathscr{B}_R$ as:

$$\boldsymbol{U} = \boldsymbol{I} + \nabla_{\overline{X}_d}\overline{\boldsymbol{u}}^{\mathrm{s}}_d \tag{61}$$

where

$$\nabla_{\overline{X}_d}\overline{\boldsymbol{u}}^s_d = \frac{1}{2}\left[\nabla_{\overline{X}_d}\overline{\boldsymbol{u}}_d + \left(\nabla_{\overline{X}_d}\overline{\boldsymbol{u}}_d\right)^T\right] \tag{62}$$

We write $\nabla_{\overline{X}_d}\overline{\boldsymbol{u}}^s_d$ in Voigt form as $\boldsymbol{\varepsilon}$. Since $\boldsymbol{\varepsilon}$ is a function of $\overline{\boldsymbol{u}}_d(\overline{\boldsymbol{X}}_d)$ and this is a function of $\overline{\boldsymbol{v}}$, we can write:

$$\boldsymbol{\varepsilon} = \boldsymbol{B}\overline{\boldsymbol{v}} \tag{63}$$

where $\boldsymbol{B}$ is a 3×18 matrix relating the strain at a given point in the element with the nodal unknowns in frame $\mathscr{B}_R$. Since the element is coupled, the $\boldsymbol{B}$ matrix can be written as a sum of three $\boldsymbol{B}$ contributions:

$$\boldsymbol{B} = \boldsymbol{B}_b + \boldsymbol{B}^0_m + \boldsymbol{B}^1_m \tag{64}$$

where the superscripts b and m indicate bending and plane terms, respectively. The membrane term is split in two parts (the constant stress part, $\boldsymbol{B}^0_m$ and the high order stress part $\boldsymbol{B}^1_m$). The element forces and stiffness are given by:

$$\overline{\boldsymbol{f}} = \int_{\mathscr{B}_0}\left(\boldsymbol{B}^T\boldsymbol{\sigma}\right)\mathrm{d}\mathscr{B}_0 \tag{65}$$

$$\overline{\boldsymbol{K}} = \int_{\mathscr{B}_0}\left(\boldsymbol{B}^T\boldsymbol{D}\boldsymbol{B}\right)\mathrm{d}\mathscr{B}_0 \tag{66}$$

[7] A linear least-square application of $\boldsymbol{\sigma}$ is used for output.

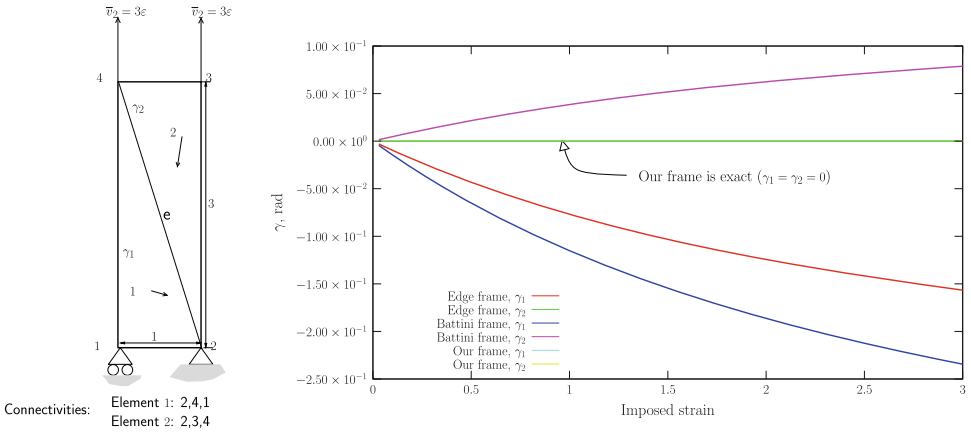

Fig. 4 Two-element pure deformation test

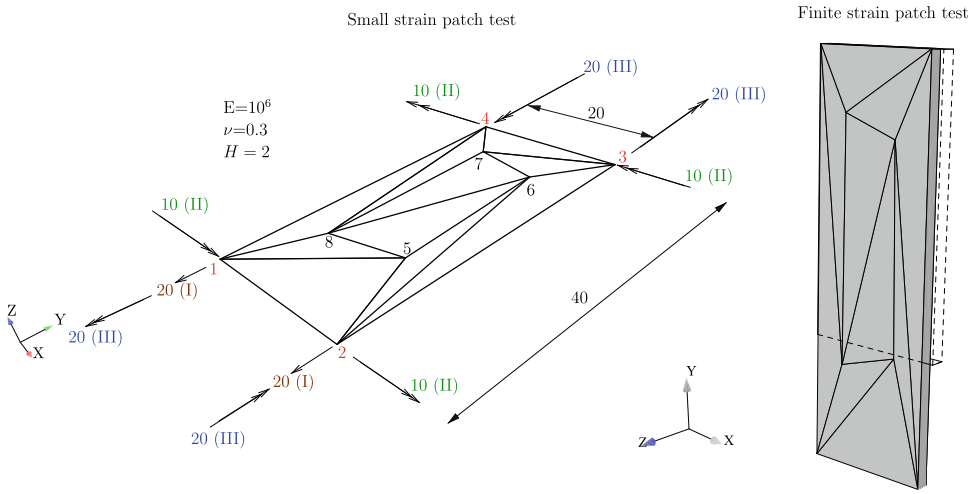

Fig. 5 Small strain and finite strain patch test: 10 irregular elements are used

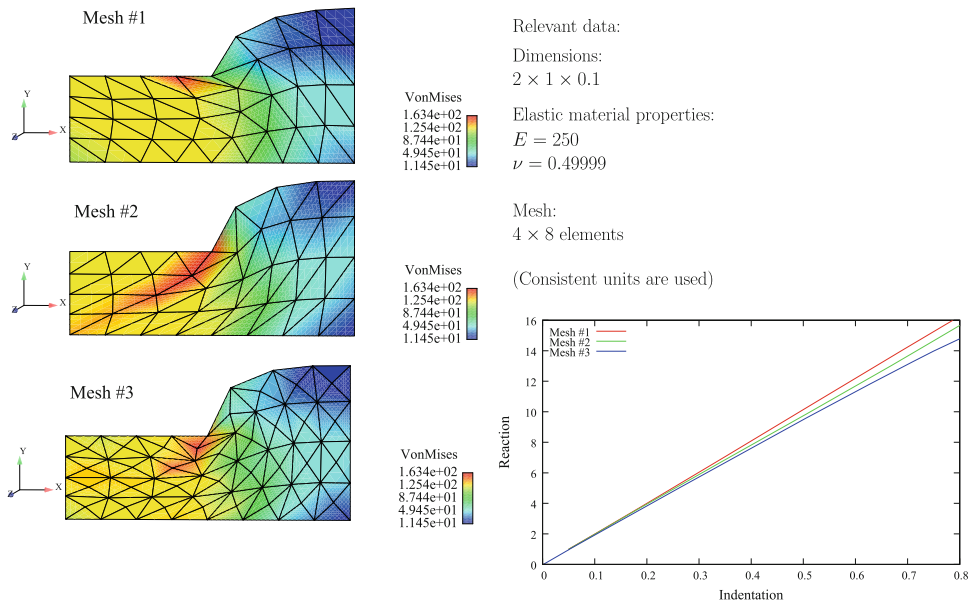

Fig. 6 Finite strain indentation test: comparison of three mesh arrangements, see also [38]

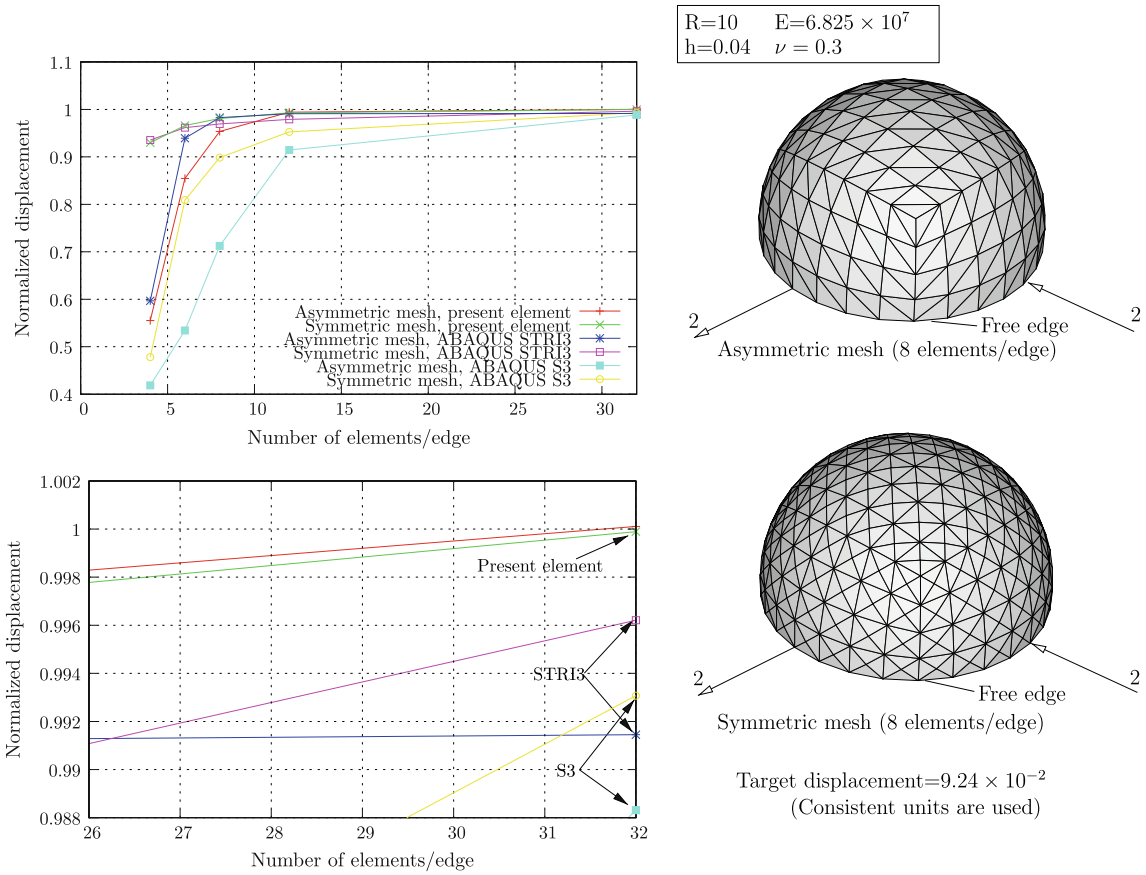

Fig. 7 Pinched hemisphere (linear elastic test): geometry, boundary conditions, material properties and convergence of the displacement under the point-loads

since

$$\frac{\mathrm{d}\boldsymbol{B}}{\mathrm{d}\overline{\boldsymbol{u}}} = \boldsymbol{0} \tag{67}$$

$$\frac{\mathrm{d}\boldsymbol{\sigma}}{\mathrm{d}\boldsymbol{\varepsilon}} = \boldsymbol{D} \tag{68}$$

3.1 Bending part

We use a combination of the classical discrete Kirchhoff plate triangle (DKT) and the quadratic interpolation proposed by Felippa and Haugen [22]. The ingredients of the original developments of the DKT triangle are:

- Transverse displacement obtained by cubic Hermite interpolation on the triangle's edges.
- Quadratic deformational rotations defined on the triangle.
- Kirchhoff conditions satisfied at the three corner nodes and mid-edge points.

We arrive at a new, much more concise form of the strain-displacement matrices. The deformational rotation field is characterized by two angles (β_x and β_y), after substitution of the Kirchhoff-Love conditions:

$$\beta_x = \beta_{x0} + \boldsymbol{p}(\boldsymbol{\xi})^T \boldsymbol{T}_{\beta_x u} \boldsymbol{u}_N \tag{69}$$

$$\beta_y = \beta_{y0} + \boldsymbol{p}(\boldsymbol{\xi})^T \boldsymbol{T}_{\beta_y u} \boldsymbol{u}_N \tag{70}$$

with $\boldsymbol{p}(\boldsymbol{\xi})^T = \{\xi_1, \xi_2, \xi_1\xi_2, \xi_1^2, \xi_2^2\}$ being the quadratic polynomial basis vector. We use area coordinates $\boldsymbol{\xi} = \{\xi_1, \xi_2\} \in [0, 1]^2$. The uniform terms β_{x0} and β_{y0} in (69,70) do not contribute to the curvature, and hence are left unspecified. The core nodal degrees-of-freedom correspond to two in-plane rotation angles at each node and are grouped as:

$$\boldsymbol{u}_N^T = \{\theta_1^x, \theta_1^y, \theta_2^x, \theta_2^y, \theta_3^x, \theta_3^y\} \tag{71}$$

A comparison with classical formulations shows that the transverse displacement is absent from the list of nodal unknowns. It is simply filtered by the corotational frame and therefore only deformational parts are present. This, along with careful coding, allows some computational savings. The matrices $\boldsymbol{T}_{\beta_x u}$ and $\boldsymbol{T}_{\beta_y u}$ in (69,70) are calculated after constraints tying the transverse displacement and the quadratic rotation field are imposed:

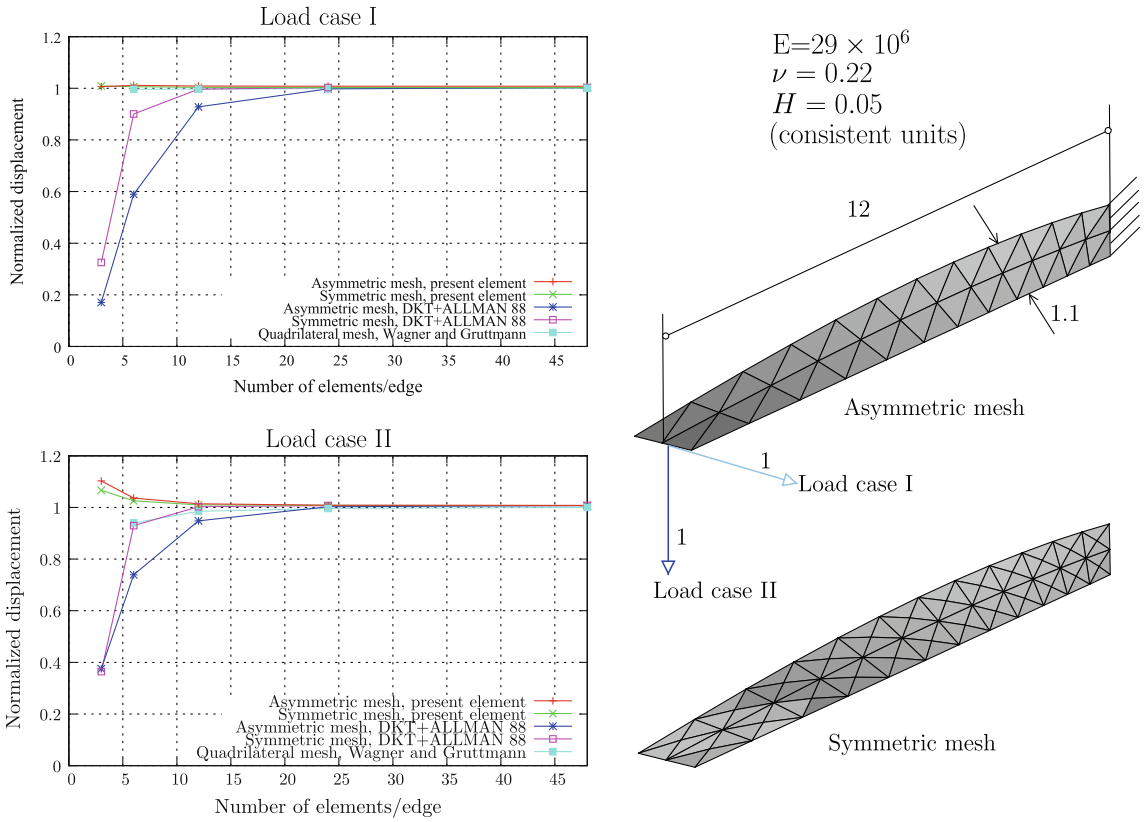

Fig. 8 Twisted beam (linear elastic test): geometry, boundary conditions, material properties and convergence of the displacement for two load cases (see also [35])

$$\boldsymbol{T}_{\beta_x u} = \begin{bmatrix} 3\hat{x}_c\hat{y}_c & 1-3\hat{x}_c^2 & 0 & 0 & 3\hat{x}_c\hat{y}_c & -1-3\hat{x}_c^2 \\ 0 & 0 & 3\hat{x}_b\hat{y}_b & 1-3\hat{x}_b^2 & 3\hat{x}_b\hat{y}_b & -1-3\hat{x}_b^2 \\ 3\hat{x}_a\hat{y}_a-3\hat{x}_c\hat{y}_c & 3\hat{x}_c^2-3\hat{x}_a^2 & 3\hat{x}_a\hat{y}_a-3\hat{x}_b\hat{y}_b & 3\hat{x}_b^2-3\hat{x}_a^2 & -3\hat{x}_b\hat{y}_b-3\hat{x}_c\hat{y}_c & 3\hat{x}_b^2+3\hat{x}_c^2 \\ -3\hat{x}_c\hat{y}_c & 3\hat{x}_c^2 & 0 & 0 & -3\hat{x}_c\hat{y}_c & 3\hat{x}_c^2 \\ 0 & 0 & -3\hat{x}_b\hat{y}_b & 3\hat{x}_b^2 & -3\hat{x}_b\hat{y}_b & 3\hat{x}_b^2 \end{bmatrix} \tag{72}$$

$$\boldsymbol{T}_{\beta_y u} = \begin{bmatrix} -1+3\hat{y}_c^2 & -3\hat{x}_c\hat{y}_c & 0 & 0 & 1+3\hat{y}_c^2 & -\hat{x}_c\hat{y}_c \\ 0 & 0 & -1+3\hat{y}_b^2 & -3\hat{x}_b\hat{y}_b & 1+3\hat{y}_b^2 & -3\hat{x}_b\hat{y}_b \\ 3\hat{x}_c^2-3\hat{x}_a^2 & 3\hat{x}_c\hat{y}_c-3\hat{x}_a\hat{y}_a & 3\hat{x}_b^2-3\hat{x}_a^2 & 3\hat{x}_b\hat{y}_b-3\hat{x}_a\hat{y}_a & -3(\hat{y}_c^2+\hat{y}_b^2) & 3\hat{x}_b\hat{y}_b+3\hat{x}_c\hat{y}_c \\ -3\hat{y}_c^2 & 3\hat{x}_c\hat{y}_c & 0 & 0 & -3\hat{y}_c^2 & 3\hat{x}_c\hat{y}_c \\ 0 & 0 & -3\hat{y}_b^2 & 3\hat{x}_b\hat{y}_b & -3\hat{y}_b^2 & 3\hat{x}_b\hat{y}_b \end{bmatrix} \tag{73}$$

where the following notation was used:

$$\hat{x}_a = \frac{x_2-x_1}{\|\boldsymbol{x}_2-\boldsymbol{x}_1\|_2} = -\frac{x_a}{l_a}$$
$$\hat{y}_a = \frac{y_2-y_1}{\|\boldsymbol{x}_2-\boldsymbol{x}_2\|_2} = -\frac{y_a}{l_a}$$
$$\hat{x}_b = \frac{x_3-x_2}{\|\boldsymbol{x}_3-\boldsymbol{x}_2\|_2} = -\frac{x_b}{l_b}$$
$$\hat{y}_b = \frac{y_3-y_2}{\|\boldsymbol{x}_3-\boldsymbol{x}_2\|_2} = -\frac{y_b}{l_b}$$
$$\hat{x}_c = \frac{x_1-x_3}{\|\boldsymbol{x}_1-\boldsymbol{x}_3\|_2} = -\frac{x_c}{l_c}$$
$$\hat{y}_c = \frac{y_1-y_3}{\|\boldsymbol{x}_1-\boldsymbol{x}_3\|_2} = -\frac{y_c}{l_c} \tag{74}$$

This is not the standard form adopted for the DKT and requires fewer operations, since the strain-displacement matrix depends on six edge coordinates and area coordinates. Note that matrices $\boldsymbol{T}_{\beta_x u}$ and $\boldsymbol{T}_{\beta_y u}$ contain the complete low and high order terms and no decoupling was adopted. The planar triangle area is determined from l_a, l_b and l_c using Heron's formula:

$$A_\triangle = \frac{1}{4}\sqrt{(l_c-l_a-l_b)(l_a-l_b-l_c)(l_a-l_b+l_c)(l_a+l_b+l_c)} \tag{75}$$

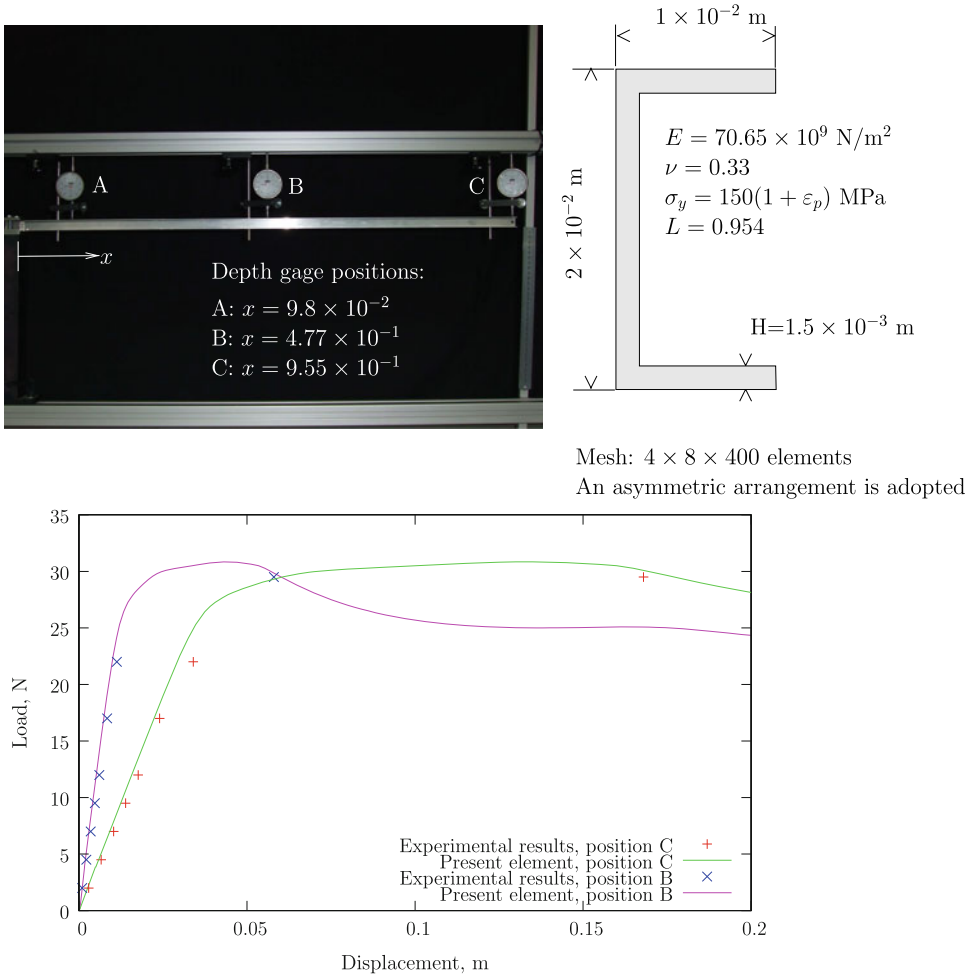

Fig. 9 Cantilever beam: experimental arrangement, cross-section dimensions and material properties

The derivatives of $\boldsymbol{p}(\boldsymbol{\xi})$ with respect to x and y are directly written as:

$$\frac{\partial \boldsymbol{p}(\boldsymbol{\xi})}{\partial \boldsymbol{x}} = \frac{1}{2A_\triangle} \begin{bmatrix} y_b & -x_b \\ y_c & -x_c \\ \xi_2 y_b + \xi_1 y_c & -\xi_2 x_b - \xi_1 x_c \\ 2\xi_1 y_b & -2\xi_1 x_b \\ 2\xi_2 y_c & -2\xi_2 x_c \end{bmatrix} \tag{76}$$

The curvatures are directly obtained from the previous relations, making use of the chain rule. These result in a 3×6 strain-DOF matrix which is given as:

$$\boldsymbol{B}_b = \frac{\xi_3 H}{2} \begin{bmatrix} \frac{\partial \boldsymbol{p}(\boldsymbol{\xi})}{\partial x}^T \boldsymbol{T}_{\beta xu} \\ \frac{\partial \boldsymbol{p}(\boldsymbol{\xi})}{\partial y}^T \boldsymbol{T}_{\beta yu} \\ \frac{\partial \boldsymbol{p}(\boldsymbol{\xi})}{\partial y}^T \boldsymbol{T}_{\beta xu} + \frac{\partial \boldsymbol{p}(\boldsymbol{\xi})}{\partial x}^T \boldsymbol{T}_{\beta yu} \end{bmatrix} \tag{77}$$

depending exclusively on ξ_1, ξ_2, ξ_3, H and the edge vectors. We remark that this is a *new form* of the DKT element and its simplicity is unmatched by classical derivations.

3.2 Membrane part

For the membrane part we modify the OPT element developed by C.A. Felippa and coworkers, originally derived using two different approaches: the EFF (Extended Free Formulation) [2] and the ANDES (Assumed Natural Deviatoric Strain) [23]. It was then verified that both the EFF and the ANDES lead to the same optimal[8] element, which seems to indicate that the optimal form is unique [21]. This element is a linear strain triangle with 3 corner nodes and 3 DOFs per node (two in-plane displacements and a drilling rotation). The membrane energy is partitioned in two: constant stress and high-order stress. The strain-displacement matrix $\boldsymbol{B}_m$ is additively calculated, in a form found by [15] which guarantees direct satisfaction of the patch test, as:

$$\boldsymbol{B}_m = \boldsymbol{B}_m^0 + \boldsymbol{B}_m^1 \tag{78}$$

where the constant stress part $\boldsymbol{B}_m^0$ is constructed to guarantee consistency, providing for convergence in the limit of

[8] Optimal only for certain mesh arrangements, since union-jack meshes typically produce less than optimal results, see also [14].

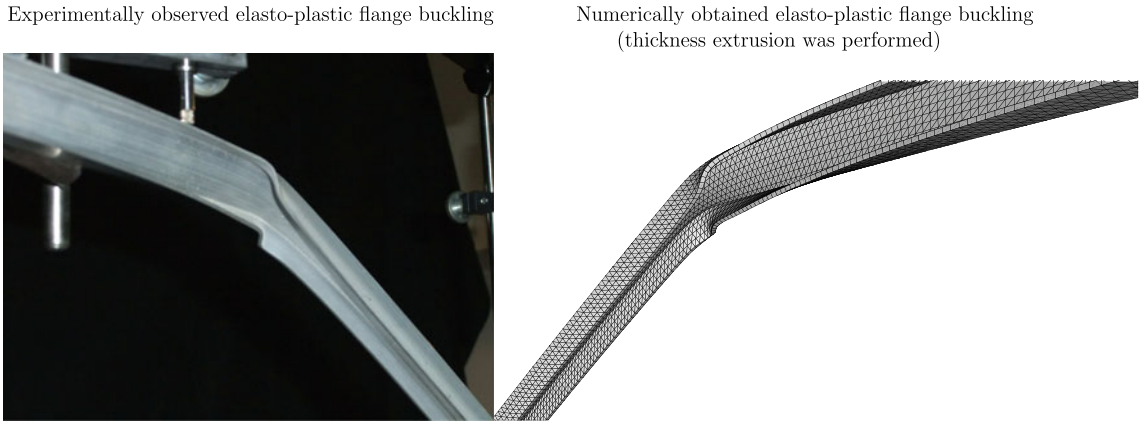

Fig. 10 Cantilever beam: comparative pictures of the elasto-plastic buckling of the flange and numerical prediction

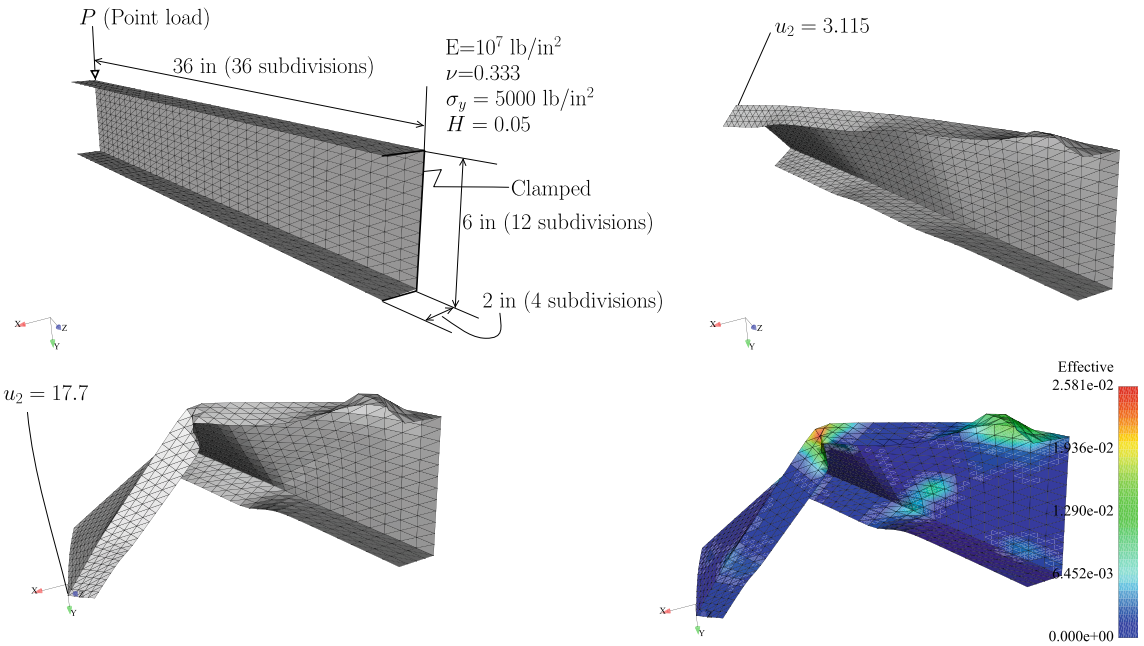

Fig. 11 Channel section cantilever beam: geometry, boundary conditions and sequence of deformed meshes. Thickness-averaged effective plastic strain is shown

mesh refinement, and the higher order part $\boldsymbol{B}_m^1$ to provide for accuracy. Both matrices involve a set of adjustable parameters which are determined by making the element reproduce the exact beam pure bending solution. The evaluation of its performance was made in [23].

3.2.1 Constant stress part

The constant stress part is directly obtained from the EFF. Although beam shape functions are used for the normal displacement, a scaling factor (α) is required since the continuum case cannot make direct use of that interpolation. Considering a constant stress state in the element, the same constant stress also exists at the boundaries. We assume a displacement field defined along the edges by beam shape functions for the normal to the edge displacement component $\tilde{u}$ and linear interpolation for the edge aligned displacement component $\tilde{v}$. For one element edge, the displacement interpolation in edge-aligned coordinates is given by ($e = a, b, c$):

$$\tilde{\boldsymbol{u}}_e = \left\{ \begin{matrix} \tilde{u} \\ \tilde{v} \end{matrix} \right\}_e = \left[\begin{matrix} N_{ue1}(\varsigma) & 0 & \alpha N_{\theta e1}(\varsigma) & N_{ue2}(\varsigma) & 0 & \alpha N_{\theta e2}(\varsigma) \\ 0 & N_{ve1}(\varsigma) & 0 & 0 & N_{ve2}(\varsigma) & 0 \end{matrix} \right] \left\{ \begin{matrix} \tilde{u}_{e1} \\ \tilde{v}_{e1} \\ \theta_{e1} \\ \tilde{u}_{e2} \\ \tilde{v}_{e2} \\ \theta_{e2} \end{matrix} \right\} \tag{79}$$

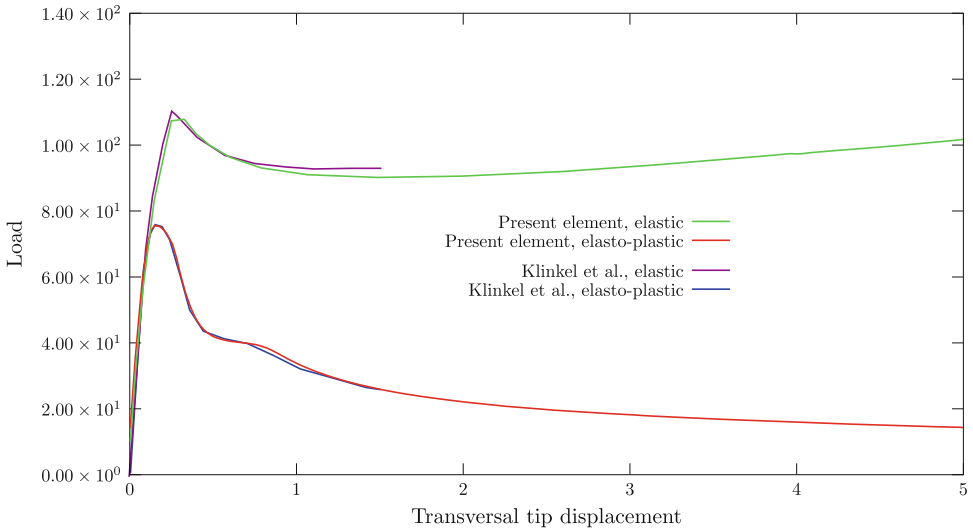

Fig. 12 Channel section cantilever beam: load-deflection curve; comparison with [28]

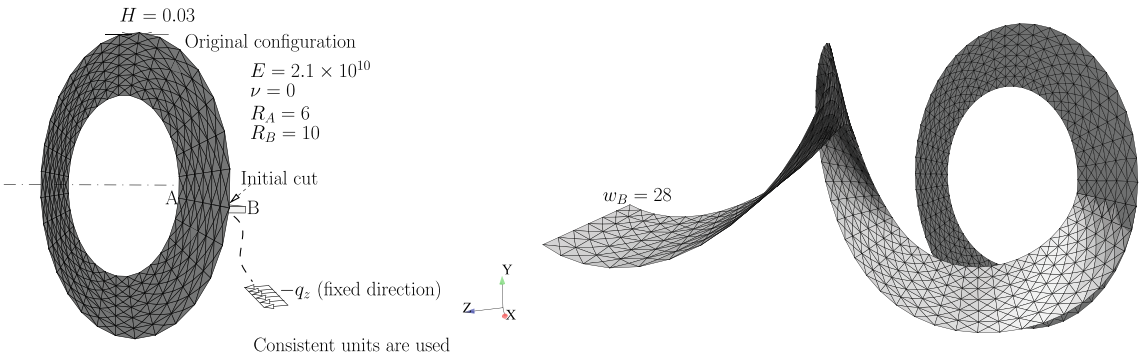

Fig. 13 Ring test by Başar and Ding [9]. Consistent units are used

where the shape functions are:

$$
\begin{aligned}
N_{ue1}(\varsigma) &= 1 - 3\varsigma^2 + 2\varsigma^3 \\
N_{\theta e1}(\varsigma) &= \varsigma - 2\varsigma^2 + \varsigma^3 \\
N_{ue2}(\varsigma) &= 3\varsigma^2 - 2\varsigma^3 \\
N_{\theta e2}(\varsigma) &= -\varsigma^2 + \varsigma^3 \\
N_{ve1}(\varsigma) &= 1 - \varsigma \\
N_{ve2}(\varsigma) &= \varsigma
\end{aligned}
\tag{80}
$$

with $\zeta \in [0, 1]$. Figure 3 clarifies this notation. Each edge in (a, b, c) has local nodes 1 and 2.

Writing the equilibrium equations for a single element with constant stress and strain, we have:

$$
A\boldsymbol{\sigma} : \delta\boldsymbol{\varepsilon} = \int_{l_a} \widetilde{\boldsymbol{t}}_a \cdot \delta\widetilde{\boldsymbol{u}}_a \mathrm{d}l_a + \int_{l_b} \widetilde{\boldsymbol{t}}_b \cdot \delta\widetilde{\boldsymbol{u}}_b \mathrm{d}l_b + \int_{l_c} \widetilde{\boldsymbol{t}}_c \cdot \delta\widetilde{\boldsymbol{u}}_c \mathrm{d}l_c \tag{81}
$$

using the edge transformation matrix:

$$
\boldsymbol{T}_{\mathrm{e}} = \begin{bmatrix} \hat{y}_e & \hat{x}_e \\ -\hat{x}_e & \hat{y}_e \end{bmatrix}, \quad e = a, b, c \tag{82}
$$

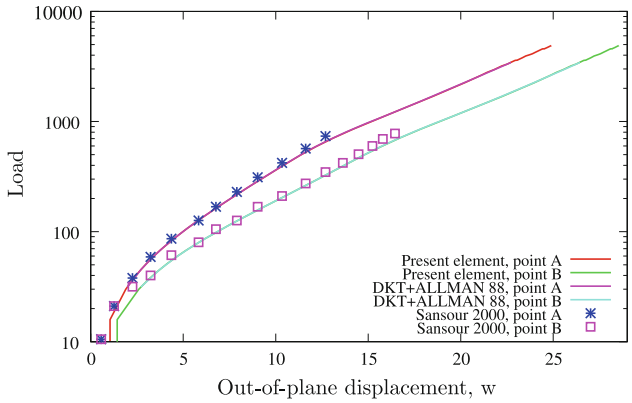

Fig. 14 Ring test: comparison with the results by Sansour et al. [33]

we finally obtain:

$$
\boldsymbol{B}_m^0 = \frac{1}{2A} \left[\begin{array}{ccc|c} y_b & 0 & \frac{\alpha}{6}(y_a - y_c)y_b & \\ 0 & -x_b & \frac{\alpha}{6}(x_a - x_c)x_b & \cdots \\ -x_b & y_b & \frac{\alpha}{3}(x_a y_a - x_c y_c) & \end{array} \right] \tag{83}
$$

This process lumps the edge stresses to balanced nodal forces, which guarantees stress equilibrium between adjacent

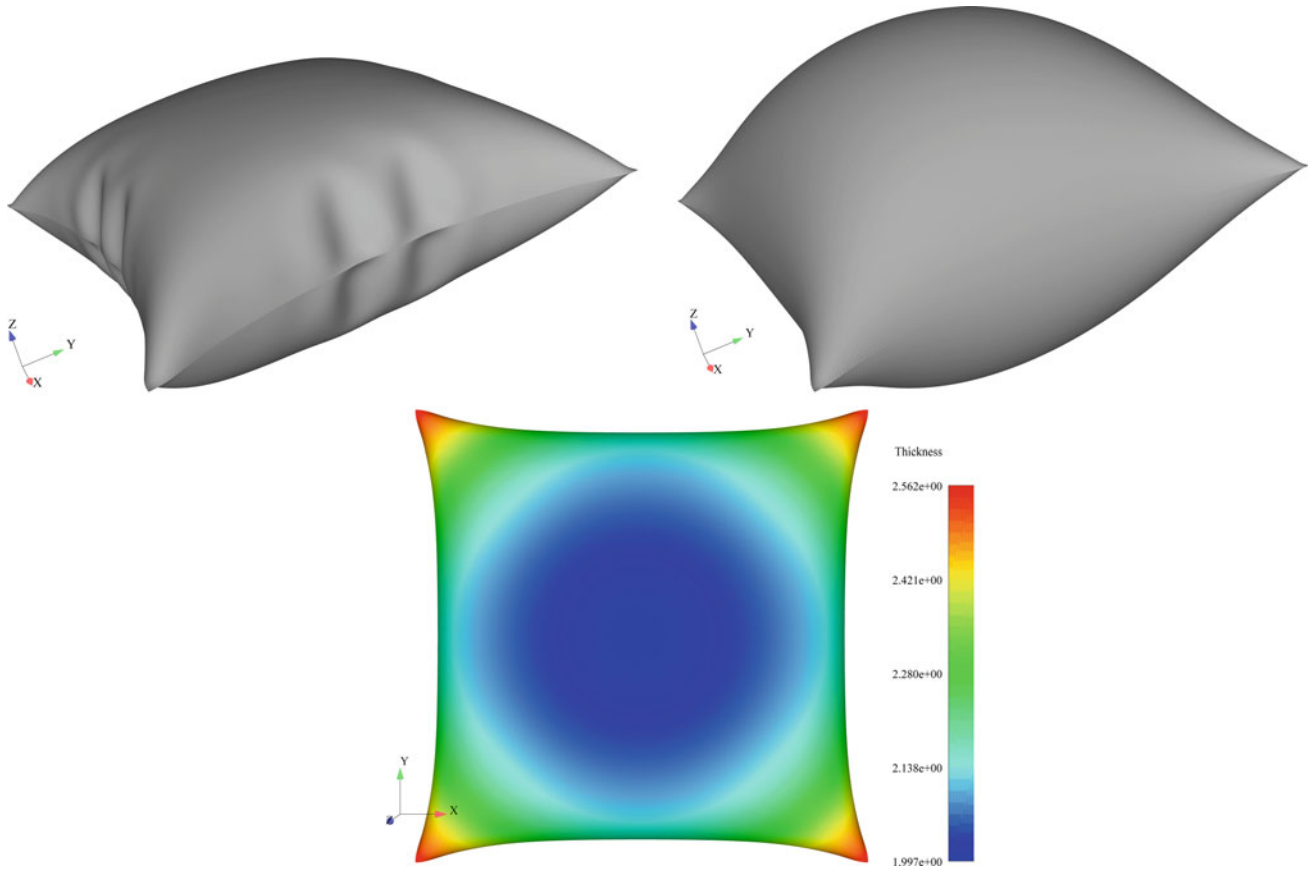

Fig. 15 Simply supported plate; neo-Hookean case, $\theta_3 = 0$ at the supports, $u_3 = 115$ and $u_3 = 185$. The thickness contour plot is also shown. Note that mirroring of the plate was employed for visualization purposes

elements for constant stress states, for any assumed displacement field. For the OPT element, the parameter α was calculated to be $3/2$.

3.2.2 Higher order stress part

The higher order part is calculated using a linear variation of the natural strains (strains aligned along median directions):

$$\boldsymbol{B}_m^1 = A\sqrt{\beta_0}\boldsymbol{T}_n\left[\xi_1\boldsymbol{Q}_1 + \xi_2\boldsymbol{Q}_2 + (1-\xi_1-\xi_2)\boldsymbol{Q}_3\right]\boldsymbol{T}_u \tag{84}$$

where $\boldsymbol{T}_n$ is the natural-global (median aligned in sharp contrast with C.A. Felippa developments) transformation matrix. The parameter β_0 is found to be $1/80$[9] and $\boldsymbol{T}_u$ is the matrix relating the hierarchical drilling rotations with the nodal degrees-of-freedom. The natural strain matrices $\boldsymbol{Q}_i, i = 1, 2, 3$ are given by:

$$\boldsymbol{Q}_1 = \begin{bmatrix} \frac{1}{l_a^2} & \frac{2}{l_a^2} & \frac{1}{l_a^2} \\ 0 & \frac{1}{l_b^2} & -\frac{1}{l_b^2} \\ -\frac{1}{l_c^2} & -\frac{1}{l_c^2} & -\frac{2}{l_c^2} \end{bmatrix} \tag{85}$$

$$\boldsymbol{Q}_2 = \begin{bmatrix} -\frac{2}{l_a^2} & -\frac{1}{l_a^2} & -\frac{1}{l_a^2} \\ \frac{1}{l_b^2} & \frac{1}{l_b^2} & \frac{2}{l_b^2} \\ -\frac{1}{l_c^2} & 0 & \frac{1}{l_c^2} \end{bmatrix} \tag{86}$$

$$\boldsymbol{Q}_3 = \begin{bmatrix} \frac{1}{l_a^2} & -\frac{1}{l_a^2} & 0 \\ -\frac{1}{l_b^2} & -\frac{2}{l_b^2} & -\frac{1}{l_b^2} \\ \frac{2}{l_c^2} & \frac{1}{l_c^2} & \frac{1}{l_c^2} \end{bmatrix} \tag{87}$$

and are obtained by assuming a beam pure bending field. For a beam in pure bending the cross sections suffer a rotation by an angle θ, and the (small) bending strain is proportional to that angle:

$$\varepsilon_b = -\frac{y}{l}\theta \tag{88}$$

where y is the distance from the neutral axis to the desired point in the transverse section and l is the initial beam length. Therefore, in (plane) pure bending the strain is proportional

[9] There is no decoupling of stiffness as proposed in the groups of C.A. Felippa and Battini, see for example [12].

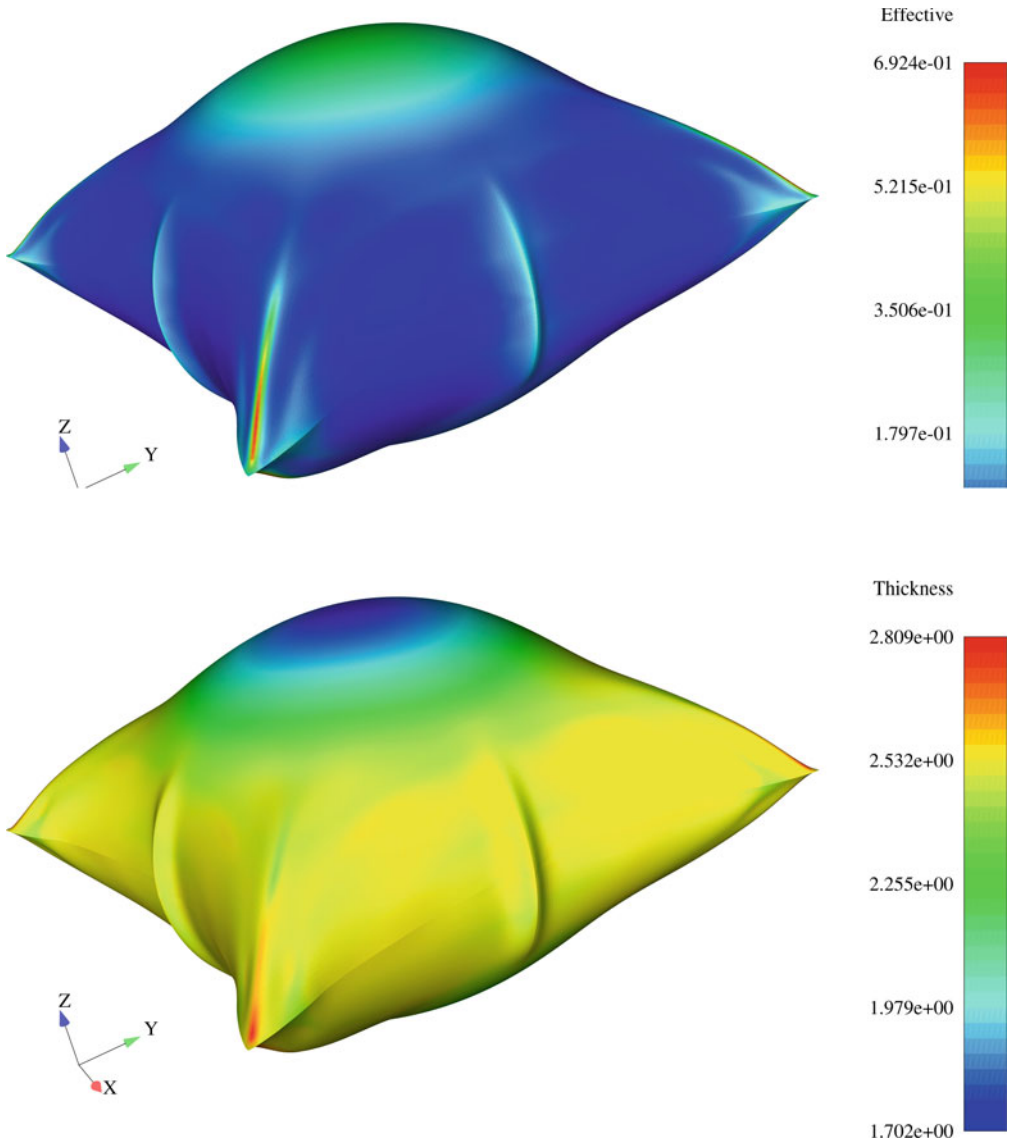

Fig. 16 Simply supported plate; elasto-plastic case: effective plastic strain and thickness contour plots. Note that mirroring of the plate was employed for visualization purposes

to a geometric factor $\frac{y}{l}$, and these factors appear in the Q_i. Q_{iab} is the strain at node i $(i = 1, 2, 3)$, parallel to side a $(a = 1, 2, 3)$, assuming that the neutral axis is parallel to side a and passing by the triangle centroid, due to the drilling rotation at node b. These are reworked expressions of those present in Ref. [2].

4 Thickness extensibility

Thickness variation is caused by the condition $\overline{\sigma}_{33} = 0$. The inaugural work of Hughes and Carnoy [26] presented this methodology, subsequently adopted in many other works such as in Dvorkin et al. [18]. Call to the constitutive library (see, e.g. [4]) makes use of four components (since $\overline{\sigma}_{13} = \overline{\sigma}_{23}$ are identically zero). For $\overline{\sigma}_{33}$ we use the Newton method to obtain:

$$\overline{\sigma}_{33}(h) = 0 \tag{89}$$

which reads (it is the iteration counter):

$$\frac{\partial \overline{\sigma}_{33}}{\partial \varepsilon_{33}} \Delta h = -\overline{\sigma}_{33} H \tag{90}$$

$$h_{it+1} \leftarrow h_{it} + \Delta h \tag{91}$$

with $h_0 = H$. Convergence of this iteration is usually achieved, for $\Delta h \leq 1 \times 10^{-8} H$, after six or seven iterations. After convergence, we calculate the tangent modulus as:

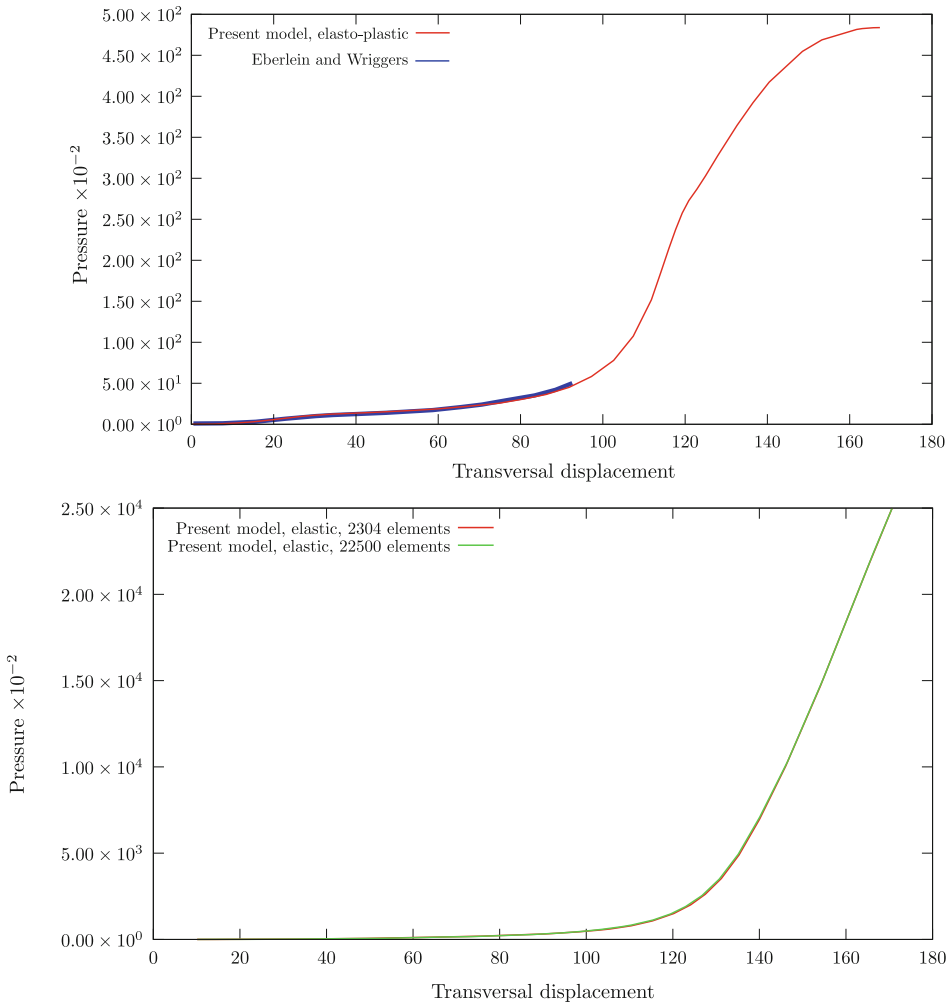

Fig. 17 Simply supported plate: pressure-displacement results. The elasto-plastic results are compared with Ref. [19]

$$\boldsymbol{C} = \frac{\partial \overline{\boldsymbol{\sigma}}}{\partial \boldsymbol{\varepsilon}} - \left(\frac{\partial \overline{\sigma}_{33}}{\partial \varepsilon_{33}}\right)^{-1} \frac{\partial \overline{\boldsymbol{\sigma}}}{\partial \varepsilon_{33}} \otimes \frac{\partial \overline{\sigma}_{33}}{\partial \boldsymbol{\varepsilon}} \tag{92}$$

Considerably more sophisticated techniques were developed by Areias et al. [7] and Wisniewski [37].

5 Numerical examples

A set of sufficiently simple examples shows:

- Correctness of the corotational formulation and satisfaction of patch and rigid-body tests.
- Accuracy of the plane and bending terms in the core element.
- Comprehensiveness of the formulation: applications in elasticity, elasto-plasticity and fracture.

The examples were run in the code created by the first Author [4]. Elasto-plasticity integration follows the recent algorithm by Areias and Rabczuk [6].

5.1 Verification tests

With the purpose of verifying the exactness of our formulation, let us first consider the two element setting shown in Fig. 4. Although the edge e identified in that Figure rotates due to stretching, the rotation angle

$$\gamma = \arctan\left(\frac{R_{R_{11}}}{R_{R_{21}}}\right) \tag{93}$$

must remain zero for $\overline{v}_2 \neq 0$. A comparison between the edge frame, Battini's [11] frame and our own is represented in Fig. 4. Although we confirm the result of Battini, who states that the corotational frame is independent of node numbering, it can be observed that his approach may produce spurious rotations. In contrast, our approach is exact. This is, to our knowledge, a new result.

Another important test is the patch-test. We here use a 10-element mesh to perform a membrane and bending patch test, as depicted in Fig. 5. Three load cases are employed (membrane forces in case I and bending moments in cases II and III) for the small strain test and membrane forces are

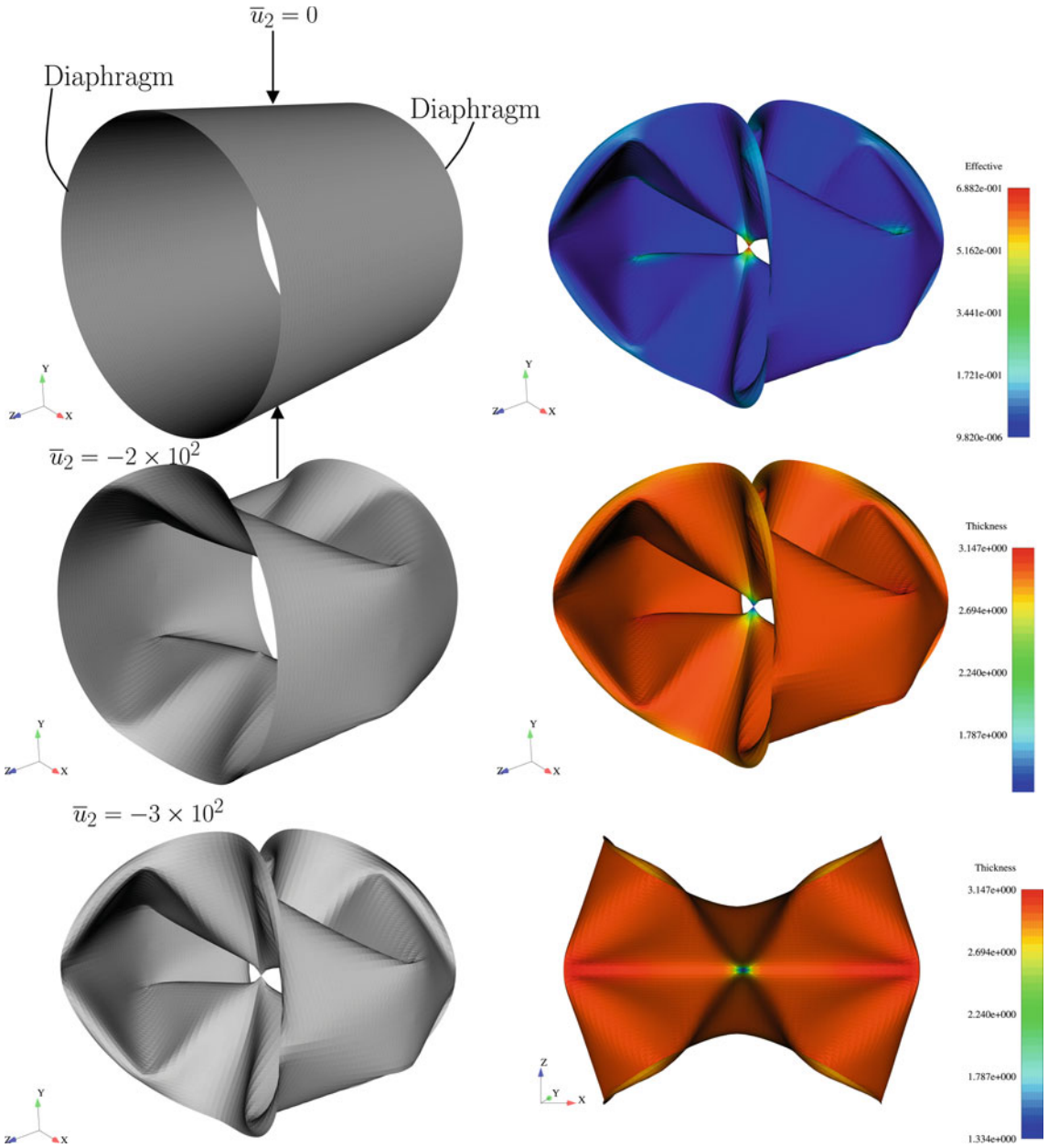

Fig. 18 Cylindrical shell with diaphragms: deformed mesh, effective plastic strain and thickness distribution

tested in finite strains. The element passes the test with constant stresses in each layer (two layers are employed).

For finite strains, we make use of the block indentation problem, recently re-tested by Wisniewski and Turska [38] to inspect the effect of three mesh arrangements in the results and also the smoothness of the von-Mises equivalent stress for a very coarse meshing. Figure 6 shows the results for this problem. Some mesh dependence can be observed, but overall the results are very good for a triangular element in near-incompressibility and similar to the typical quadrilaterals used in this test (for the three mesh arrangements).

5.2 Linear elastic pinched hemisphere

The hemispherical shell with four pinching forces is considered (see Fig. 7). We compare two triangular elements from Abaqus 6.8 (S3 and STRI3) with the present formulation for two mesh topologies (a symmetric mesh with crossed triangles and an asymmetric mesh). Note that meshes with crossed triangles were found to be inadequate for the Bergan and Felippa [14] element since a optimal parameter was not found for their Free Formulation. The results are shown in the same Fig. 7. The present element converges quicker than both elements tested in Abaqus 6.8 for the symmetric mesh.

In addition, for the finer mesh, we obtain results closer to the target value (we adopt W.K. Liu et al. 9.24×10^{-2} consistent units [30]). Results for the asymmetric mesh are also very good for sufficiently refined meshes.

5.3 Linear elastic twisted beam

The linear elastic twisted beam was considered in the benchmark proposal by MacNeal and Harder [31] and was subsequently modified by Jetteur [27]. We use the latter version in this work, since it is now more common and revealing. The test involves both out-of-plane and in-plane bending strains and is suitable to assess the effect of the in-plane element choice in the results. Unit shear in two orthogonal directions is considered. The target values for the displacement were taken from Wagner and Gruttmann [35] as 1.387 (load case I) and 0.3429 (load case II), see also Fig. 8. For a sufficiently fine mesh we obtained similar values (for a 192×32 element mesh, 1.401 and 0.3459 respectively). Figure 8 shows that our element obtained very good results when compared with a DKT plate combined with Allman's formulation [1] and similar to the quadrilateral from Ref. [35].

5.4 Clamped beam: comparison with experimental results

A slender beam with a C profile made from ductile aluminum[10] was clamped to our laboratory frame as shown in Fig. 9. The loading strategy was very simple: 2 N, 2.5 N and 5 N disks were added to a hook hanged at a drilling in the beam and depth comparators were set above the beam. We employed a non-linear least-square code to determine the elasticity modulus. The hardening law was, in contrast, estimated by trial-and-error. Elasto-plastic buckling occurs at the flanges as shown in Fig. 10. Comparative results for the proposed element are also shown in Fig. 9.

The predictive capability was found to be very good. However, further research into the hardening law will further improve the proximity between experimental results and the numerical experiments for higher displacement values.

5.5 Channel section beam

The channel section cantilever beam by Eberlein and Wriggers [19] is reproduced here. Recently, Klinkel et al. [28] tested this problem with a hybrid quadrilateral, although to a lower deformation than in the original paper. Relevant data is shown in Fig. 11 where deformed and undeformed meshes are shown for a sequence of steps. We subdivide each quadrilateral element in [28] with four triangles. The load-deflection results are shown in Fig. 12 and compared with Ref. [28].

[10] Specifically window-frame aluminum.

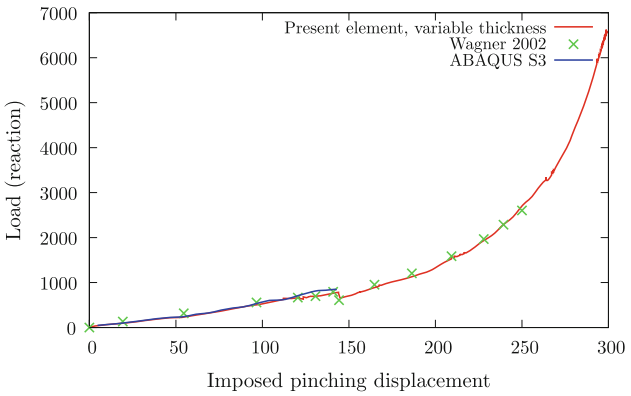

Fig. 19 Cylindrical shell with diaphragms: load-deflection results, compared with a four-node quadrilateral implementation, Ref. [36] and Abaqus S3 element

Reasonable agreement with the reported results in [28] can be observed.

5.6 Nonlinear smooth problems

The first smooth plate is the ring test first proposed by Başar and Ding [9] to test formulations for finite rotations in shells. The relevant geometry, boundary conditions and elastic properties are depicted in Fig. 13. We extend the ring up to 28 consistent units. Figure 13 depicts this extension. A comparison with the results by Sansour and Kollmann [33] is also shown in Fig. 14. We can observe that with our method we attain a higher value of ring extension and slightly more flexible results. Between the present element and a combination of DKT and Allman's element, no differences were noted, in contrast with what was observed in the linear tests. A simply-supported square plate with initial dimensions $508 \times 508 \times 2.54$ (consistent units) is loaded by a uniform, motion-dependent pressure. In this test, both compressible neo-Hookean and perfect elasto-plastic materials are considered. Constitutive properties are: $E = 69 \times 10^4$, $\nu = 0.3$ and $\sigma_y = 248$. The in-plane motion at the supports is left free. The neo-Hookean case uses zero drilling rotations at the supports (see Fig. 15). Results are shown for both cases in Figs. 15, 16 and 17. This problem puts to test the bending behavior at the earlier stages of deformation and then membrane behavior in the latter stages (see Ref. [19] for a description). During deformation, the plate corners fold and strong thickness variation occurs. A comparison with results from Ref. [19] is shown in Fig. 17 with excellent agreement. We are, however, able to reach higher deformations.

We now consider the cylinder shell with diaphragms. This test was first considered by Simo and Kennedy [34] with slightly different dimensions. The present form of the test is currently in use by many authors. It consists of a cylinder shell with the hardening law $\sigma_y = 24.3 + 300\varepsilon_p$ (consistent units)

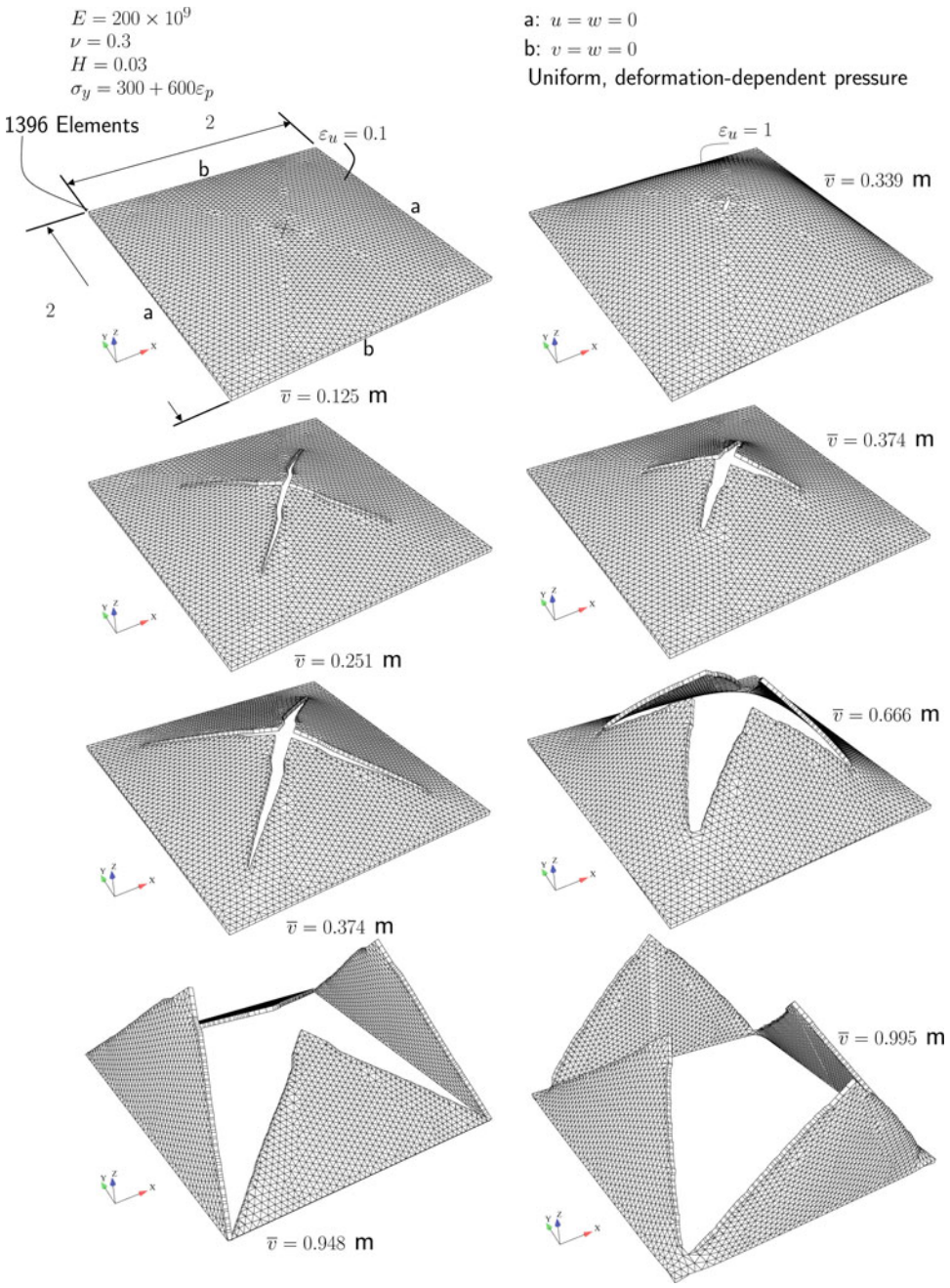

Fig. 20 Fracture process of a simply-supported plate with elasto-plastic behavior. Two cases are shown: $\varepsilon_u = 0.1$ and $\varepsilon_u = 1$. Thickness extrusion along the directors was performed

subject to two inward diametrically opposing radial loads. Elasticity modulus and Poisson coefficient are $E = 3000$ consistent units and $\nu = 0.3$, respectively. The total length of the cylinder is 600 for a radius of 300 consistent units. The initial shell thickness is $H = 3$ consistent units. Due to symmetry, only one-eighth of the cylinder needs to be modeled. Free edges have diaphragms (only rotations and longitudinal displacement are allowed). Displacement control is used: a total displacement of 300 consistent units is applied and the reactions monitored. This displacement corresponds to the total radius and is *considerably more* than what is usually published (see what was achieved by alternative approaches in [19,36]). The reason for this is the presence of a slight load decrease for a pinching displacement of around 140 which decreases the convergence radius of Newton's method. Since this problem involves large displacements and large plastic strains, as well as strong thickness gradients near the pinched point, it is a very demanding test. Large strain warping and severe relative rotations occur between elements, as can be observed in Fig. 18. For comparison, reported load-deflection

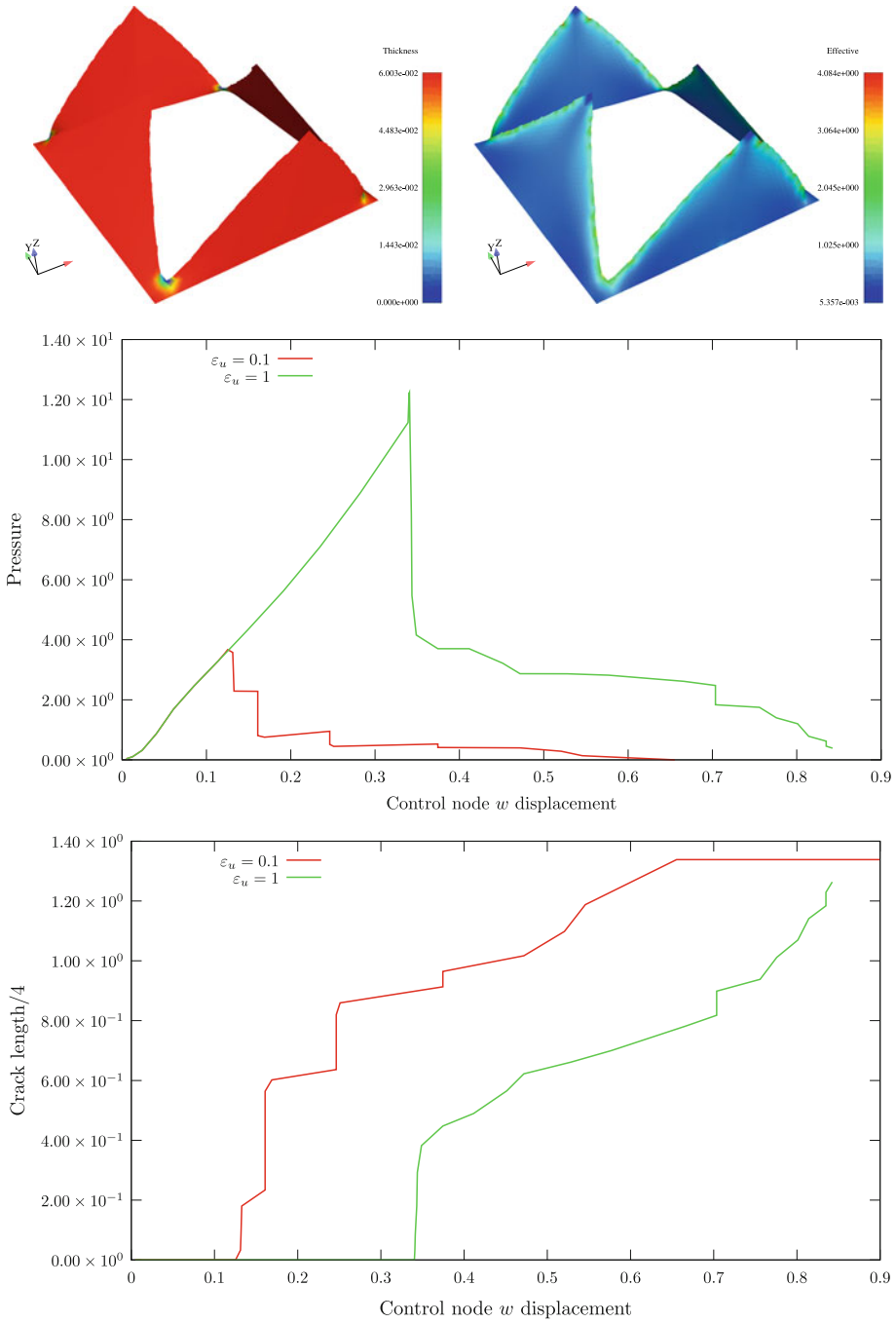

Fig. 21 Fracture process of a simply-supported plate with elasto-plastic behavior: contour plots, pressure/control node displacement and displacement/crack length results

results by Wagner et al. [36] are shown in Fig. 19. Note that these Authors reported results only up to 250 consistent units. The same 16×16 subdivided mesh as in [36] is used here for results comparison, but a finer, 32×32 subdivision mesh is required to obtain a smooth distribution of thickness and effective plastic strain. The latter is used solely for purposes of graphical representation in Fig. 18. The load-deflection results are shown in Fig. 19: results are slightly more flexible than the ones in Ref. [28].

5.7 Ductile fracture of a simply-supported plate

The fracture process of a simply-supported (all displacement components prescribed) square (2×2 consistent units) plate under pressure is tested in the following example. A single mesh containing 1396 elements is used. We use a simplistic prototype ductile fracture model with the sole purpose of showing the capabilities of our formulation (a further detailed model can be consulted in [8]). The effective plastic strain is

used as an indicator for crack propagation, when the effective plastic strain overcomes the ultimate strain, $\overline{\varepsilon}_p > \varepsilon_u$, cracks grow. Two values of ε_u are tested ($\varepsilon_u = 0.1$ and $\varepsilon_u = 1.0$) with the corresponding sequences of deformed meshes being shown in Fig. 20. The recently developed ALE method by Areias et al. [5] was adapted for a curved surface and maintains excellent mesh quality, as a careful inspection of the Figure reveals. A variant of a ductile fracture model (cf. [8]) is employed. For good visualization of the 3D director motion, an extrusion along the directors was used. Perfect kinematics and very stable crack paths can be observed (Fig. 21).

6 Conclusions

This work presented a new corotational method (both an exact frame and a new coupled core element are introduced), exactly linearized, capable of dealing with finite strain problems, including plasticity and fracture. The frame uses a complete polar decomposition which involves a closed-form $2D$ polar decomposition and shifted coordinates. Core matrices are based on a re-formulation of the DKT element for plate bending and a modified OPT element for membrane deformations. Examples show excellent performance in a variety of situations: linear benchmarks, finite strain elasticity, finite strain elasto-plasticity and fracture. An extension of this work consists in using a constrained-ALE method (we recently proposed a 2D version of the ALE-based fracture method [5]) to satisfy the shell mid-surface constraint.

Acknowledgments The authors gratefully acknowledge financing from the "Fundação para a Ciência e a Tecnologia" under the Project PTDC/EME-PME/108751 and the Program COMPETE FCOMP-01-0124-FEDER-010267.

References

1. Allman DJ (1988) Evaluation of the constant strain triangle with drilling rotations. Int J Numer Methods Eng 26:2645–2655
2. Alvin K, de la Fuente HM, Haugen B, Felippa CA (1992) Membrane triangles with corner drilling freedoms: I. The EFF element. Finite Elem Anal Des 12:165–187
3. Antman SS (2005) Nonlinear problems of elasticity, 2nd edn. Springer, New York
4. Areias P Simplas. http://home.uevora.pt/~pmaa/SimplasWebsite/Simplas.html
5. Areias P, Dias-da-Costa D, Alfaiate J, Júlio E (2009) Arbitrary bi-dimensional finite strain cohesive crack propagation. Comput Mech 45(1):61–75
6. Areias P, Rabczuk T (2010) Smooth finite strain plasticity with non-local pressure support. Int J Numer Methods Eng 81:106–134
7. Areias P, Ritto-Corrêa M, Martins JAC (2010) Finite strain plasticity, the stress condition and a complete shell model. Comput Mech 45:189–209
8. Areias P, Van Goethem N, Pires EB (2010) A damage model for ductile crack initiation and propagation. Comput Mech (in Press)
9. Basar Y, Ding Y (1992) Finite rotation shell elements for the analysis of finite rotation shell problems. Int J Numer Methods Eng 34:165–169
10. Batoz J-L (1980) A study of three-node triangular plate bending elements. Int J Numer Methods Eng 15:1771–1812
11. Battini J-M (2004) On the choice of local element frame for corotational triangular shell elements. Commun Numer Methods Eng 20:819–825
12. Battini J-M, Pacoste C (2006) On the choice of the linear element for corotational triangular shells. Comput Method Appl Mech Eng 195:6362–6377
13. Belytschko T, Liu Wk, Moran B (2000) .Nonlinear finite elements for continua and structures Wiley, New York
14. Bergan PG, Felippa CA (1985) A triangular membrane element with rotational degrees of freedom. Comput Methods Appl Mech Eng 50:25–69
15. Bergan PG, Nygaard MK (1984) Finite elements with increased freedom in choosing shape functions. Int J Numer Methods Eng 20:643–663
16. Brank B, Ibrahimbegovic A (2001) On the relation between different parametrizations of finite rotations for shells. Eng Comput 18:950–973
17. Crisfield MA, Moita GF (1996) A unified co-rotational framework for solids, shells and beams. Int J Solids Struct 33(20–22):2969–2992
18. Dvorkin E, Pantuso D, Repetto E (1995) A formulation of the MITC4 shell element for finite strain elasto-plastic analysis. Comput Methods Appl Mech Eng 125:17–40
19. Eberlein R, Wriggers P (1999) Finite element concepts for finite elastoplastic strains and isotropic stress response in shells: theoretical and computational analysis. Comput Methods Appl Mech Eng 171:243–279
20. Felippa CA (2003) A study of optimal membrane triangles with drilling freedoms. Technical report CU-CAS-03-02, University of Colorado, College of Engineering, Campus Box 429, Boulder, Colorado 80309, February 2003
21. Felippa CA, Alexander S (1992) Membrane triangles with corner drilling freedoms: III. Implementation and performance evaluation. Finite Elem Anal Des 12:203–239
22. Felippa CA, Haugen B (2005) Unified formulation of small-strain corotational finite elements: I. Theory. Comput Methods Appl Mech Eng 194:2285–2335
23. Felippa CA, Militello C (1992) Membrane triangles with corner drilling freedoms: II. The ANDES element. Finite Elem Anal Des 12:189–201
24. Goldstein H, Poole CP, Safko JL (2001) Classical mechanics, 3rd edn. Addison-Wesley, New York
25. Hughes TJR (2000) The finite element method. Dover, 2000. Reprint of Prentice-Hall edition, 1987
26. Hughes TJR, Carnoy E (1983) Nonlinear finite element formulation accounting for large membrane stress. Comput Methods Appl Mech Eng 39:69–82
27. Jetteur P (1987) Improvement of the quadrilateral jet shell element for a particular class of shell problems. Technical report IREM Internal Report 87/1, Ecole Polytechnique Fédérale de Lausanne
28. Klinkel S, Gruttmann F, Wagner W (2008) A mixed shell formulation accounting for thickness strains and finite strain 3D material models. Int J Numer Methods Eng 74:945–970
29. Korelc J (2002) Multi-language and multi-environment generation of nonlinear finite element codes. Eng Comput 18(4):312–327
30. Liu WK, Guo Y, Belytschko T (1998) A multiple-quadrature eight-node hexahedral finite element for large deformation elastoplastic analysis. Comput Methods Appl Mech Eng 154:69–132
31. MacNeal RH, Harder RL (1985) A proposed standard set of problems to test finite element accuracy. Finite Elem Anal Des 1:1–20

32. Wolfram Research Inc. Mathematica (2007). http://www.wolfram.com/mathematica/
33. Sansour C, Kollmann FG (2000) Families of 4-node and 9-node finite elements for a finite deformation shell theory. an assessment of hybrid stress, hybrid strain and enhanced strain elements. Comput Mech 24:435–447
34. Simo JC, Kennedy JG (1992) On the stress resultant geometrically exact shell model. Part V: nonlinear plasticity: formulation and integration algorithms. Comput Methods Appl Mech Eng 96: 133–171
35. Wagner W, Gruttmann F (2005) A robust non-linear mixed hybrid quadrilateral shell element. Int J Numer Methods Eng 64:635–666
36. Wagner W, Klinkel S, Gruttmann F (2002) Elastic and plastic analysis of thin-walled structures using improved hexahedral elements. Comput Struct 80:857–869
37. Wisniewski K (1998) A shell theory with independent rotations for relaxed Biot stress and right stretch strain. Comput Mech 21(2):101–122
38. Wisniewski K, Turska E (2009) Improved 4-node Hu-Washizu elements based on skew coordinates. Comput Struct 87:407–424